Distinct inactive conformations of the dopamine D2 and D3 receptors correspond to different extents of inverse agonism

J. Robert Lane[1,2*], Ara M. Abramyan[3], Pramisha Adhikari[3], Alastair C. Keen[1,2,4], Kuo-Hao Lee[3], Julie Sanchez[1,2], Ravi Kumar Verma[3], Herman D. Lim[4], Hideaki Yano[3], Jonathan A. Javitch[5,6*], Lei Shi[3*]

[1]Division of Pharmacology, Physiology and Neuroscience, School of Life Sciences, Queen's Medical Centre, University of Nottingham, Nottingham NG7, 2UH, U.K.

[2]Centre of Membrane Protein and Receptors, Universities of Birmingham and Nottingham, United Kingdom.

[3]Computational Chemistry and Molecular Biophysics Unit, National Institute on Drug Abuse - Intramural Research Program, National Institutes of Health, Baltimore, Maryland, United States

[4]Drug Discovery Biology, Department of Pharmacology and Medicinal Chemistry, Monash Institute of Pharmaceutical Sciences, Monash University (Parkville campus), Parkville, Victoria, Australia

[5]Departments of Psychiatry and Pharmacology, Vagelos College of Physicians and Surgeons, Columbia University, New York, New York, United States

[6]Division of Molecular Therapeutics, New York State Psychiatric Institute, New York, New York, United States

[*]Corresponding authors:

Email: lei.shi2@nih.gov (LS), Rob.Lane@nottingham.ac.uk (JRL), jaj2@cumc.columbia.edu (JAJ)

ABSTRACT

By analyzing and simulating inactive conformations of the highly-homologous dopamine D_2 and D_3 receptors (D_2R and D_3R), we find that eticlopride binds D_2R in a pose very similar to that in the D_3R/eticlopride structure but incompatible with the D_2R/risperidone structure. In addition, risperidone occupies a sub-pocket near the Na^+ binding site, whereas eticlopride does not. Based on these findings and our experimental results, we propose that the divergent receptor conformations stabilized by Na^+-sensitive eticlopride and Na^+-insensitive risperidone correspond to different degrees of inverse agonism. Moreover, our simulations reveal that the extracellular loops are highly dynamic, with spontaneous transitions of extracellular loop 2 from the helical conformation in the D_2R/risperidone structure to an extended conformation similar to that in the D_3R/eticlopride structure. Our results reveal previously unappreciated diversity and dynamics in the inactive conformations of D_2R. These findings are critical for rational drug discovery, as limiting a virtual screen to a single conformation will miss relevant ligands.

Impact Statement

The occupation of a sub-pocket near the Na^+-binding site in D_2R by the Na^+-insensitive antagonists is the structural basis for their greater inverse agonism than that of the Na^+-sensitive ligands.

Keywords

Dopamine D_2 receptor, Na^+ sensitivity, inverse agonism, molecular dynamics.

47 **INTRODUCTION**

48 G protein-coupled receptors (GPCRs) are important therapeutic targets for numerous human
49 diseases. Our understanding of GPCR functional mechanisms has evolved from a simple
50 demarcation of single active and inactive states to the appreciation and detection of multiple active
51 states responsible for partial or biased agonism (Latorraca et al., 2017; Venkatakrishnan et al.,
52 2013; Weis and Kobilka, 2018). High-resolution crystal structures of these proteins are vital for
53 structure-based (rational) drug discovery (RDD) efforts designed to tailor selectivity and efficacy
54 (Congreve et al., 2014; Michino et al., 2015a). While considerable efforts have been directed at
55 the development of biased agonists that couple preferentially to a particular effector pathway
56 (Free et al., 2014; Manglik et al., 2016; McCorvy et al., 2018), less attention has been dedicated
57 to the possibility that different antagonist scaffolds with differing efficacy of inverse agonism might
58 lead to different receptor conformations and hence different "inactive" states. Such a possibility
59 could have a major impact on RDD for antagonists, since a GPCR crystal structure stabilized by
60 a particular antagonist might represent an invalid docking target for an antagonist that prefers a
61 different inactive conformation. Although substantial differences in antagonist binding mode and
62 position of the binding pockets have been revealed among different aminergic receptors, no
63 conformational differences has been detected for the inactive state in any individual aminergic
64 receptor (Michino et al., 2015a). In particular, although a number of antagonists derived from
65 different scaffolds have been co-crystallized with the β_2 adrenergic receptor, conformational
66 differences among these crystal structures are minimal (Michino et al., 2015a).

67 Curiously, the inactive state structures of the highly homologous dopamine D2 and D3
68 receptors (D_2R and D_3R) revealed substantial differences on the extracellular side of the
69 transmembrane domain, especially in TM6 (Figure 1), when bound with antagonists derived from
70 different scaffolds (Chien et al., 2010; Wang et al., 2018). Specifically, the D_3R structure is in
71 complex with eticlopride, a substituted benzamide (PDB: 3PBL) (Chien et al., 2010), while the
72 D_2R structure is bound with risperidone, a benzisoxazole derivative (PDB: 6CM4) (Wang et al.,

73 2018). The binding poses of the two ligands differ substantially. Risperidone is oriented relatively
74 perpendicular to the membrane plane with its benzisoxazole ring penetrating into a hydrophobic
75 pocket beneath the orthosteric binding site (OBS) of D_2R; in contrast, eticlopride is oriented
76 relatively parallel to the membrane plane and contacts the extracellular portion of TM5 in D_3R, a
77 sub-pocket that risperidone does not occupy in D_2R (Sibley and Shi, 2018; Wang et al., 2018).
78 Nemonapride, another substituted benzamide, binds in the OBS of the slightly divergent D_4R
79 (PDB: 5WIV) (Wang et al., 2017) in a manner very similar to that of eticlopride in the D_3R (Sibley
80 and Shi, 2018).

81 Importantly, the co-crystalized ligands (risperidone, eticlopride, and nemonapride) display little
82 subtype selectivity across D_2R, D_3R, and D_4R (Chien et al., 2010; Hirose and Kikuchi, 2005;
83 Silvestre and Prous, 2005; Wang et al., 2017) (also see PDSP database (Roth et al., 2000)).
84 Given the high homology among these D_2-like receptors, especially between D_2R and D_3R, the
85 drastic conformational differences between the inactive state structures of these receptors may
86 be better explained by different binding poses of antagonists bearing different scaffolds rather
87 than inherent differences in the receptors. Thus, we hypothesized that different antagonist
88 scaffolds may favor distinct inactive conformations of D_2R. To test this hypothesis, we carried out
89 extensive molecular dynamics (MD) simulations of D_2R in complex with non-selective antagonists
90 derived from different scaffolds to characterize the plasticity of the OBS and the extracellular loop
91 dynamics in the inactive conformational state.

92 **RESULTS**

93 **The Ile$^{3.40}$ sub-pocket is occupied by risperidone and spiperone but not eticlopride in D_2R**

94 Compared to eticlopride bound in the D_3R structure, risperidone in the D_2R structure
95 penetrates deeper into the binding site, with its benzisoxazole moiety occupying a sub-pocket that
96 eticlopride does not reach. By examining the D_2R/risperidone structure, we found that the
97 benzisoxazole moiety is enclosed by 8 residues in D_2R, which are identical among all D_2-like
98 receptors (i.e., D_2R, D_3R, and D_4R): Cys118$^{3.36}$ (superscripts denote Ballesteros-Weinstein
99 numbering (Ballesteros and Weinstein, 1995)), Thr119$^{3.37}$, Ile122$^{3.40}$, Ser197$^{5.46}$, Phe198$^{5.47}$,
100 Phe382$^{6.44}$, Trp386$^{6.48}$, and Phe390$^{6.52}$. Notably, three of these residues (Ile122$^{3.40}$, Phe198$^{5.47}$,
101 and Phe382$^{6.44}$) on the intracellular side of the OBS that we previously defined (Michino et al.,
102 2015a), accommodate the F-substitution at the tip of the benzisoxazole ring in a small cavity
103 (termed herein as the Ile$^{3.40}$ sub-pocket) (Figure 2a). Both Ile122$^{3.40}$ and Phe382$^{6.44}$ of this Ile$^{3.40}$
104 sub-pocket are part of the conserved Pro$^{5.50}$-Ile$^{3.40}$-Phe$^{6.44}$ motif that undergoes rearrangement
105 upon receptor activation (Rasmussen et al., 2011), and we have found that the I122$^{3.40}$A mutation
106 renders D_2R non-functional (Klein Herenbrink et al., 2019; Wang et al., 2018). Interestingly, this
107 Ile$^{3.40}$ sub-pocket is collapsed in both the D_3R and D_4R structures (Sibley and Shi, 2018) (Figure
108 2b,c). We noted that this collapse is associated with rotation of the sidechain of Cys$^{3.36}$: In the
109 D_2R/risperidone structure, the sidechain of Cys$^{3.36}$ faces the OBS, whereas in the D_3R/eticlopride
110 and D_4R/nemonapride structures, it rotates downwards to partially fill the Ile$^{3.40}$ sub-pocket (Figure
111 2a-c).

112 To test our hypothesis that these observed differences in the crystal structures are due to the
113 binding of antagonists bearing different scaffolds but not intrinsic divergence of D_2-like receptors,
114 we compared the binding modes of three non-selective antagonists in D_2R. We reverted three
115 thermostabilizing mutations introduced for crystallography (I122$^{3.40}$A, L375$^{6.37}$A, and L379$^{6.41}$A)
116 back to their WT residues, established WT D_2R models in complex with risperidone, spiperone,

117 or eticlopride, and carried out extensive MD simulations (see Methods, Figure 1 – figure
118 supplement 1 and Table 1).

119 In our prolonged MD simulations of the WT D_2R/risperidone complex (>65 μs, Table 1), we
120 observed that risperidone stably maintains the binding pose captured in the crystal structure, even
121 without the thermostabilizing mutations (Figure 2d). Thus, the I122$^{3.40}$A mutation has minimal
122 impact on the binding pose of risperidone. Interestingly, in the simulations of the WT D_2R model
123 in complex with spiperone, a butyrophenone derivative, the F-substitution on the butyrophenone
124 ring similarly occupies the Ile$^{3.40}$ sub-pocket as risperidone (Figure 2e). Note that the F-
125 substitutions in risperidone and spiperone are located at similar distances to the protonated N
126 atoms that interact with Asp$^{3.32}$ (measured by the number of carbon atoms between them, Figure
127 1 – figure supplement 1) and these two ligands appear to be optimized to occupy the Ile$^{3.40}$ sub-
128 pocket.

129 In contrast, in our simulations of the D_2R/eticlopride complex, the eticlopride pose revealed in
130 the D_3R structure (PDB: 3PBL) is stable throughout the simulations and does not protrude into
131 the Ile$^{3.40}$ sub-pocket (Figure 2f). Consistent with the difference in the crystal structures noted
132 above (Figure 2a,b), when risperidone and spiperone occupy the Ile$^{3.40}$ sub-pocket, the sidechain
133 of Cys118$^{3.36}$ rotates away with its χ1 rotamer in *gauche-*, while in the presence of the bound
134 eticlopride, this rotamer is stable in *trans* (Figure 2 – figure supplement 1).

135 To validate these computational findings regarding the occupation of the Ile$^{3.40}$ sub-pocket,
136 we mutated Ile122$^{3.40}$ of WT D_2R to both Trp and Ala and characterized how these mutations
137 affect the binding affinities for spiperone, risperidone, and eticlopride (Table 2). We hypothesized
138 that the bulkier sidechain of Trp at position 3.40 would hamper the binding of spiperone and
139 risperidone since they occupy the Ile$^{3.40}$ sub-pocket but have no effect on eticlopride binding, while
140 the smaller Ala should not affect the binding of spiperone or risperidone. Consistent with this
141 hypothesis, the I122W mutation decreased the binding affinities of risperidone (13-fold) and
142 spiperone (6-fold) compared to WT but had no effect on that of eticlopride. In contrast, the I122A

143 mutation did not affect the affinities of spiperone or risperidone, which is consistent with our
144 simulation results that show the I122A mutation has minimal impact on risperidone binding. In
145 contrast, I122A caused a 3-fold increase in the affinity of eticlopride, suggesting that the I122A
146 mutation may promote an inactive conformation of D_2R that favors eticlopride binding. Together
147 these results support our proposal that different antagonist scaffolds may favor distinct inactive
148 conformations of D_2R.

149 **Occupation of the Ile$^{3.40}$ sub-pocket confers insensitivity to Na^+ in antagonist binding**

150 Ligand binding in D_2-like receptors can be modulated by Na^+ bound in a conserved allosteric
151 binding pocket coordinated by Asp$^{2.50}$ and Ser$^{3.39}$ (Michino et al., 2015b; Neve, 1991; Wang et al.,
152 2017). Note that the aforementioned Cys$^{3.36}$ and Ile$^{3.40}$ are adjacent to the Na^+ coordinating Ser$^{3.39}$;
153 thus, we further hypothesized that the occupation of the Ile$^{3.40}$ sub-pocket by spiperone or
154 risperidone makes them insensitive to Na^+. To test this hypothesis, we simulated D_2R/risperidone,
155 D_2R/spiperone, D_2R/eticlopride, and D_2R/(-)-sulpiride complexes in the presence versus absence
156 of bound Na^+ (Table 1). Interestingly, the occupancy of the Ile$^{3.40}$ sub-pocket by either spiperone
157 or risperidone was unaffected by the presence or absence of bound Na^+ (Figure 2 – figure
158 supplement 1). In contrast, while the poses of eticlopride and (-)-sulpiride are highly stable in the
159 presence of bound Na^+, they oscillated between different poses in the absence of Na^+. These
160 oscillations are associated with the sidechain of Cys$^{3.36}$ swinging back and forth between the two
161 rotamers, suggesting an important role of Na^+ binding in stabilizing the poses of eticlopride and
162 (-)-sulpiride and the configuration of the Ile$^{3.40}$ sub-pocket (Figure 2 – figure supplement 1).
163 Interestingly, the previous MD simulations described by Wang et al. indicated that nemonapride's
164 binding pose in D_4R is more stable in the presence of bound Na^+ as well (Wang et al., 2017).

165 Consistent with these computational results, we have previously shown that spiperone binding
166 is insensitive to the presence of Na^+, while the affinities of eticlopride and sulpiride are increased
167 in the presence of Na^+ (Michino et al., 2015b). In this study, we performed binding experiments in

168 the absence or presence of Na^+ and found the affinity of risperidone to be unaffected, in
169 accordance with this hypothesis (Table 2).

170 Together these findings support our hypothesis that the ability of a ligand to bind the $Ile^{3.40}$
171 sub-pocket relates with its sensitivity to Na^+ in binding, due to allosteric connections between the
172 sub-pocket and the Na^+ binding site.

173 **Functional consequences of distinct antagonist-bound inactive conformations.**

174 To further investigate the functional impact of these conformational differences surrounding
175 the OBS, we used a bioluminescence resonance energy transfer (BRET) assay, which measures
176 conformational changes of the Go protein heterotrimer following activation by D_2R (Michino et al.,
177 2017), to evaluate the inverse agonism activities of several representative D_2R ligands. These
178 ligands can be categorized into two groups according to their sensitivities to Na^+ in binding at D_2R,
179 which have been characterized either in our current study or in previous studies (Michino et al.,
180 2015b; Neve, 1991; Newton et al., 2016). While risperidone, spiperone, and (+)-butaclamol have
181 been found to be insensitive to Na^+ in binding, (-)-sulpiride, eticlopride, and raclopride show
182 enhanced binding affinities in the presence of Na^+. Using quinpirole as a reference full agonist,
183 we found that the Na^+ insensitive ligands display significantly greater inverse agonism (< -30%
184 that of the maximal response of quinpirole) relative to the Na^+ sensitive ligands (> -15% that of
185 the maximal response of quinpirole, Figure 3). These observations are consistent with findings
186 from earlier [^{35}S]GTPγS binding experiments of Roberts and Strange in which (+)-butaclamol,
187 risperidone, and spiperone were found to inhibit significantly more [^{35}S]GTPγS binding than
188 raclopride and (-)-sulpiride (Roberts and Strange, 2005). Of note, these [^{35}S] GTPγS binding
189 experiments were performed in the absence of Na^+.

190 Based on these functional data together with the different binding modes revealed by our
191 computational simulations, we propose that ligands that occupy the $Ile^{3.40}$ sub-pocket exhibit a
192 greater level of inverse agonism as compared to those that do not. Therefore, across the tested

193 inverse agonists there is a negative relation between ligand sensitivity to Na^+ and the extent of
194 inverse agonism at D_2R. The differential occupation of the $Ile^{3.40}$ sub-pocket is the structural basis
195 for the Na^+ sensitivity, which contributes significantly to the extent of inverse agonism of the tested
196 ligands.

197 **Plasticity of the ligand binding site propagates to affect the overall receptor conformation**

198 By occupying the $Ile^{3.40}$ sub-pocket, the benzisoxazole moiety of risperidone pushes the
199 conserved $Phe^{6.52}$ away from the binding site in the D_2R/risperidone structure compared to its
200 position in the D_3R/eticlopride structure. This interaction is responsible for positioning the aromatic
201 cluster of TM6 and TM7 ($Trp^{6.48}$, $Phe^{6.51}$, $Phe^{6.52}$, $His^{6.55}$, and $Tyr^{7.35}$) in D_2R differently from its
202 configurations in the D_3R and D_4R structures, resulting in an overall outward positioning of the
203 extracellular portion of TM6 in D_2R (Figure 4 – figure supplement 1). On the extracellular side of
204 the OBS, the space near $Ser^{5.42}$ and $Ser^{5.43}$ that accommodates the bulky substitutions of the
205 benzamide rings of the bound eticlopride and nemonapride in the D_3R and D_4R structures is not
206 occupied by risperidone in D_2R, which is likely associated with the inward movement of the
207 extracellular portion of TM5 in D_2R relative to those in the D_3R and D_4R structures (Figure 1).

208 To evaluate whether these conformational rearrangements are due to the minor divergence
209 in these regions of the receptors or to the ligand binding site plasticity that accommodates ligands
210 bearing different scaffolds, we compared the resulting conformations of D_2R bound with
211 risperidone or eticlopride. We observed the same trend of rearrangements of the transmembrane
212 segments surrounding the OBS in the resulting receptor conformations from our D_2R/risperidone
213 and D_2R/eticlopride simulations (Figure 4a), i.e., an inward movement of TM6 and outward
214 movement of TM5 in the presence of the bound eticlopride (Figure 4b,c). Without such
215 movements in D_2R/eticlopride, $Ser193^{5.42}$ and $Ser194^{5.43}$ would clash with the bound eticlopride
216 (Figure 4a). These findings further support our inference that differences between the D_2R and
217 D_3R inactive structures are largely due to the different scaffolds of the bound non-selective ligands.

218 **The extracellular loop 2 (EL2) of D_2R/risperidone can spontaneously unwind**

219 In addition to differences in the transmembrane segments surrounding the OBS, there are
220 also substantial differences in the configuration of EL2 in the D_2R and D_3R structures. EL2
221 between TM4 and TM5 is connected to TM3 via a disulfide bond formed between $Cys^{EL2.50}$ (see
222 Methods and Figure 5 – figure supplement 1 for the indices of EL1 and EL2 residues) and $Cys^{3.25}$.
223 The conformation of EL2, the sequence of which is not conserved among aminergic GPCRs, is
224 expected to be dynamic. Indeed, in the D_2R/risperidone structure, the sidechains of residues
225 $176^{EL2.40}$, $178^{EL2.46}$, $179^{EL2.47}$, and $180^{EL2.48}$, which are distal to the OBS were not solved, likely due
226 to their dynamic nature. Curiously, the portion of EL2 C-terminal to $Cys182^{EL2.50}$ (residues
227 $182^{EL2.50}$-$186^{EL2.54}$), which forms the upper portion of the OBS that is in contact with ligand, is in a
228 helical conformation in the D_2R/risperidone structure.

229 Strikingly, in our MD simulations of D_2R complexes, we found that this helical region showed
230 a tendency to unwind (Video 1). The unwinding of EL2 involves a drastic rearrangement of the
231 sidechain of $Ile183^{EL2.51}$, which dissociates from a hydrophobic pocket formed by the sidechains
232 of $Val111^{3.29}$, $Leu170^{4.60}$, $Leu174^{EL2.38}$, and $Phe189^{5.38}$. Specifically, the unwinding process is
233 initiated by the loss of a hydrogen-bond (H-bond) interaction between the sidechain of $Asp108^{3.26}$
234 and the backbone amine group of $Ile183^{EL2.51}$ formed in the D_2R/risperidone structure (Figure 5 –
235 figure supplement 2b, step i). When this interaction is broken, the orientation of residues $182^{EL2.50}$-
236 $186^{EL2.54}$ deviates markedly from that of the crystal structure, losing its helical conformation (see
237 below). Subsequently, the sidechain of $Ile183^{EL2.51}$ rotates outwards and passes a small steric
238 barrier of $Gly173^{EL2.37}$ (Figure 5 – figure supplement 2b, step ii), and in some trajectories makes
239 a favorable hydrophobic interaction with the sidechain of $Ala177^{EL2.45}$. In a few long trajectories,
240 $Ile183^{EL2.51}$ rotates further towards the extracellular vestibule where it can make favorable
241 interactions with hydrophobic or aromatic residues from the N terminus, or the bound risperidone
242 (Supplementary Movie 1). Consequently, residues $182^{EL2.50}$-$186^{EL2.54}$ are in a fully extended loop
243 conformation while $Ile184^{EL2.52}$ tilts under EL2 (Figure 5 – figure supplement 2b, step iii).

244 In the D_3R structure, the aligned residue for Asp108$^{3.26}$ of D_2R is conserved as Asp104$^{3.26}$; its
245 sidechain forms an interaction not with Ile182$^{EL2.51}$ but rather with the sidechain of Asn173$^{EL2.39}$,
246 which is also conserved in D_2R as Asn175$^{EL2.39}$. In the D_4R, the aligned two residues (Asp109$^{3.26}$
247 and Asn175$^{EL2.39}$) are conserved as well, their sidechains are only 4.3 Å away in the D_4R structure,
248 a distance slightly larger than the 3.2 Å in the D_3R structure. Even though these residues are
249 conserved in D_2R, the interaction in D_3R (and potentially in D_4R), between Asp$^{3.26}$-Asn$^{EL2.39}$, is not
250 present in the D_2R structure in which the aligned Asn175$^{EL2.39}$ faces lipid (Figure 5 – figure
251 supplement 2a). However, in a few of our long D_2R simulations, Asn175$^{EL2.39}$ gradually moves
252 inwards and approaches Asp108$^{3.26}$ (Figure 5 – figure supplement 2b, step iv). At this point, the
253 EL2 conformation of D_2R is highly similar to that of D_3R (Figure 5 – figure supplement 2c),
254 suggesting that EL2 is dynamic and can exist in both conformations.

255 We evaluated the tendency of the EL2 helix to unwind in each of the simulated D_2R complexes
256 by measuring the stability of the backbone H-bond between Ile183$^{EL2.51}$ and Asn186$^{EL2.54}$, a key
257 stabilizing force of the helix (Figure 5a). When we plotted the Ile183$^{EL2.51}$-Asn186$^{EL2.54}$ distance
258 against the Asp108$^{3.26}$-Ile183$^{EL2.51}$ distance for each D_2R complex (Figure 5b), we found that the
259 loss of the Asp108$^{3.26}$-Ile183$^{EL2.51}$ interaction increases the probability of breaking the Ile183$^{EL2.51}$-
260 Asn186$^{EL2.54}$ H-bond, i.e., the unwinding of EL2. Interestingly, in all our simulated D_2R complexes,
261 EL2 has a clear tendency to unwind, regardless of the scaffold of the bound ligand (Figure 5c,d,
262 Videos 1 and 3). Note that in the D_3R/eticlopride simulations, the aligned residues Ser182$^{EL2.51}$
263 and Asn185$^{EL2.54}$ do not form such a H-bond, and EL2 is always in an extended conformation
264 (Figure 5b-d). This tendency of EL2 to transition towards the extended conformation is also
265 present in our simulations of D_2R in complex with a partial agonist, aripiprazole, whereas EL2 in
266 the D_3R complexes with partial agonists (R22 and S22) remains in the extended conformation
267 (Table 1 and Figure 5 – figure supplement 3). Interestingly, Asp104$^{3.26}$ and Ser182$^{EL2.51}$ can move
268 into interacting range in the D_3R/eticlopride simulations, and the Ser182$^{EL2.51}$-Asn185$^{EL2.54}$
269 interaction can sporadically form in the D_3R/R22 simulations – both raise the possibility that the

270 extended conformation of D_3R EL2 may transition to a helical conformation.

271 Interestingly, in one of our long MD trajectories of the D_2R/risperidone complex, EL2 evolved
272 into a conformation that has a helical N-terminal portion and an extended C-terminal portion
273 (Video 4 and Figure 5 – figure supplement 4). This conformation is not observed in either of the
274 D_2R/risperidone and D_3R/eticlopride structures but is similar to that of the 5-$HT_{2A}R$/risperidone
275 structure, further demonstrating the dynamics of this loop region (Figure 5 – figure supplement 4).

276 In marked contrast to the obvious trend toward unwinding of EL2 in all our simulated D_2R
277 complexes, in our recent simulations of MhsT, a transporter protein with a region found by
278 crystallography to alternate between helical and unwound conformations (Malinauskaite et al.,
279 2014), we failed to observe any spontaneous unwinding over a similar simulation timescale (with
280 the longest simulations being ~5-6 μs) when the region was started from the helical conformation
281 (Abramyan et al., 2018; Stolzenberg et al., 2017). This shows how difficult it can be to capture
282 known dynamics in simulations and suggests that the C-terminal helical conformation of EL2 in
283 D_2R represents a higher energy state than the extended conformation, which allows for
284 observation of the transitions in a simulation timescale not usually adequate to sample
285 folding/unfolding events (Piana et al., 2011).

286 **Both the EL2 conformation and ligand scaffold affect the EL1 conformation.**

287 We have previously shown that the divergence in both the length and number of charged
288 residues in EL1 among D_2R, D_3R, and D_4R is responsible for the selectivity of more extended
289 ligands (Michino et al., 2013; Newman et al., 2012). Another striking difference in the D_2R, D_3R,
290 and D_4R structures is the position of the conserved $Trp^{EL1.50}$ in EL1. $Trp100^{EL1.50}$ is in a much more
291 inward position in the D_2R structure, making a direct contact with the bound risperidone (Figure
292 6a), $Trp101^{EL1.50}$ in D_4R interacts with the bound nemonapride that has an extended structure,
293 whereas $Trp96^{EL1.50}$ in D_3R is not in contact with eticlopride (Figure 6b). Thus, we asked whether
294 these distinct positions of $Trp^{EL1.50}$ are due to the divergence in EL1 among these receptors

295 (Michino et al., 2013) or due to the multiple inactive conformations that differentially accommodate
296 the binding of non-selective ligands of divergent scaffolds.

297 When residues $182^{EL2.50}$-$186^{EL2.54}$ of EL2 are in a helical conformation, in the D_2R/risperidone
298 simulations, we found that there is more room in the extracellular vestibule and the position of
299 $Trp100^{EL1.50}$ is flexible and can adopt several positions and orientations (Figure 6c,e,f). In the
300 D_2R/eticlopride simulations, $Trp100^{EL1.50}$, which cannot interact with eticlopride, shows more
301 flexibility than that observed in the presence of risperidone and can move to a similar position like
302 that of $Trp96^{EL1.50}$ in the D_3R structure (Figure 6 – figure supplement 1 and Video 2). Interestingly,
303 in this position, the conformation of $Trp^{EL1.50}$ can be stabilized by the disulfide bond of EL2 (Ioerger
304 et al., 1999) (as shown in Video 2) or by interaction with the N terminus, which was truncated in
305 the receptor construct used in the determination of the crystal structure. In the D_2R/spiperone
306 simulations, the phenyl substitution on the triazaspiro[4.5]decane moiety protrudes towards the
307 interface between TM2 and TM3, and contacts $Trp100^{EL1.50}$, which is flexible as well and can
308 adopt a position that is even further away from the OBS than that of $Trp96^{EL1.50}$ in the D_3R structure
309 (Figure 6 – figure supplement 1).

310 In contrast, when EL2 is in an extended conformation like that in D_3R, it restricts the flexibility
311 of $Trp100^{EL1.50}$ (Video 3). This trend is consistent with the D_3R/eticlopride simulations in which we
312 do not observe any significant rearrangement of $Trp96^{EL1.50}$ (Figure 6d,e,f).

313 Thus, we infer that the distinct conformation of $Trp100^{EL1.50}$ in the D_2R structure is a combined
314 effect of the helical EL2 conformation and the favored interaction that $Trp100^{EL1.50}$ can form with
315 the bound risperidone in the crystal structure, the latter of which however, has a limited influence
316 on the binding affinity of risperidone (Wang et al., 2018), consistent with the unstable interaction
317 between risperidone and $Trp100^{EL1.50}$ in our simulations (Figure 6, Video 2). Indeed, in the fully
318 extended EL2 conformation in which $Ile183^{EL2.51}$ rotates to face the extracellular vestibule,
319 $Ile183^{EL2.51}$ makes a direct contact with the bound risperidone, whereas $Trp100^{EL1.50}$ loses its
320 interaction with the ligand entirely (Video 1). Nevertheless, risperidone retains all other contacts

321 in the OBS. In the recently reported 5-HT_{2A}R/risperidone structure (PDB: 6A93) (Kimura et al.,
322 2019), risperidone has a very similar pose in the OBS as that in the D_2R structure, occupying the
323 Ile$^{3.40}$ sub-pocket as well. However, on the extracellular side of the OBS, EL2 in the 5-
324 HT_{2A}R/risperidone complex is in an extended conformation and the EL2 residue Leu228$^{EL2.51}$
325 contacting risperidone aligns to Ile183$^{EL2.51}$ of D_2R, whereas the conserved Trp141$^{EL1.50}$ does not
326 interact with risperidone in the 5-HT_{2A}R. It is tempting to speculate that the EL2 and EL1 dynamics
327 we observe in the D_2R/risperidone simulations represents a more comprehensive picture, as the
328 divergent interactions shown in the extracellular loops of the 5-HT_{2A}R/risperidone and
329 D_2R/risperidone structures may not result from differences in the protein sequences of this
330 dynamic region between these two receptors but rather two different static snapshots due to
331 differences in the crystallographic conditions (Note risperidone has similarly high affinities for both
332 D_2R and 5HT_{2A}R (Kimura et al., 2019; Wang et al., 2018)).
333 Thus, the plasticity of the OBS and the dynamics of the extracellular loops appear to be two
334 relatively separated modules in ligand recognition. To the extent of our simulations, we did not
335 detect strong ligand-dependent bias in the EL2 dynamics as we did for the OBS. However, when
336 EL2 is helical, the EL1 dynamics are sensitive to the bound ligand (compare Figure 6 and Figure
337 6 – figure supplement 1); when EL2 is extended, it restricts EL1 dynamics (Figure 6).

338 **The Ile184$^{EL2.50}$-Trp100$^{EL1.50}$ interaction is not critical for risperidone binding.**

339 To further investigate the dynamics and coordination of EL2 and EL1 loops, we mutated
340 Leu94$^{2.64}$, Trp100$^{EL1.50}$, and Ile184$^{EL2.50}$, and evaluated the effects of the L94A, W100A, and I184A,
341 mutations on the binding affinities of eticlopride, risperidone, and spiperone. As shown in Figure
342 6 – figure supplement 2, Leu94$^{2.64}$ and Trp100$^{EL1.50}$ are closely associated in both the D_2R and
343 D_3R structures, while Ile184$^{EL2.50}$ interacts with Trp100$^{EL1.50}$ only in the D_2R structure. In our time-
344 resolved energy transfer (Tr-FRET) binding experiments, using a fluorescently labelled spiperone
345 derivate (spiperone-d2) as a tracer ligand, we found that both L94A and W100A significantly

346 reduced the affinities of all antagonists, whereas I184A only reduced the affinity of eticlopride
347 while it improved that of risperidone (Table 3). Thus, the effects of the L94A and W100A mutations
348 have similar trends, which appear independent of the effect of I184A. Indeed, for Trp100 to switch
349 between the positions in the D_2R and D_3R structures, it must pass the steric hinderance of the
350 sidechain of Leu94; thus, some effects of the L94A mutation may reflect its perturbation of the
351 positioning of Trp100, and vice versa.

352 These findings support our conclusions that the close interaction between Ile184$^{EL2.50}$ and
353 Trp100$^{EL1.50}$ revealed by the D_2R/risperidone crystal structure is not necessary for the stabilization
354 of the risperidone pose. Indeed, in our simulations, EL2 has significant intrinsic dynamics and
355 transitions from the helical to unwound conformation independent of the bound ligands (see
356 above). When it is in an extended conformation, Ile184 is dissociated from Trp100.

357 **The clustering of the binding site conformations.**

358 Virtual screening has been widely used as an initial step in drug discovery for novel ligand
359 scaffolds. To this end, we found that D_2R can significantly change its binding site shape to
360 accommodate antagonists bearing different scaffolds, while EL2 is intrinsically dynamic. Thus, it
361 is necessary to comprehensively consider the binding site conformations in virtual screening
362 campaigns against D_2R, because limiting the screening to only a single conformation will miss
363 relevant ligands. Indeed, the strategy of ensemble docking, in which each ligand is docked to a
364 set of receptor conformers, has been adapted in recent virtual screening efforts (Amaro et al.,
365 2018).

366 To characterize the OBS conformational ensemble sampled by D_2R in complex with ligands
367 bearing different scaffolds in the context of EL2 dynamics, we clustered the OBS conformations
368 in our representative D_2R/eticlopride and D_2R/risperidone MD trajectories in which EL2
369 transitioned from helical to unwound conformations (see Methods). As expected, the OBS
370 conformations in these two complexes are significantly different and can be easily separated into

371 distinct clusters. For the clustering results shown in Table 4, the average pairwise RMSDs of the
372 OBS residues (apRMSDs, see Methods) between the D_2R/eticlopride and D_2R/risperidone
373 clusters are >1.1 Å, which are similar to that between the D_2R and D_3R structures (1.2 Å), while
374 the apRMSDs within each cluster is smaller than those between any two clusters (Figure 7).
375 Interestingly, at this level of clustering, when the two clusters for each complex are ~0.8-0.9 Å
376 apRMSD away from each other, the extended and helical conformations of EL2 are always mixed
377 in a cluster (Table 4). This observation suggests that the helical versus extended EL2
378 conformations are not closely associated with the OBS conformations.

379 Thus, while the centroid frames from each cluster can form an ensemble for future virtual
380 screening for the primary scaffold occupying the OBS, in order to discover novel prolonged
381 ligands that protrude out of the OBS to interact with EL2 and EL1 residues (Michino et al., 2015a),
382 additional frames that cover both helical and extended EL2 conformations from each cluster will
383 have to be used to screen for the optimal extensions of the primary scaffold.

384 **DISCUSSION**

385 Our results highlight unappreciated conformational complexity of the inactive state of GPCRs
386 and suggest that the risperidone bound D_2R structure represents only one of a number of possible
387 inactive conformations of D_2R. Critically, this conformation is incompatible with the binding of other
388 high affinity D_2R ligands such as eticlopride. While distinct conformational states responsible for
389 functional selectivity have garnered great attention, the potential existence of divergent inactive
390 conformations is of critical importance as well. By combining *in silico* and *in vitro* findings, we
391 propose that occupation of the $Ile^{3.40}$ sub-pocket by antagonists confers a distinct D_2R
392 conformation that is associated with both a greater degree of inverse agonism and Na^+
393 insensitivity in binding, such that Na^+ sensitivity is negatively related with the extent of inverse
394 agonism for the tested ligands. However, other structural elements may also contribute to the
395 extent of inverse agonism (Zhang et al., 2014). Regardless, the distinct inactive conformations
396 stabilized by antagonists with different scaffolds may reflect different degrees of inactivation.

397 In addition to advancing our mechanistic understanding of receptor function, our findings have
398 implications for high-throughput virtual screening campaigns, as important hits would be missed
399 by focusing on a single inactive state captured in a crystal structure that is stabilized by an
400 antagonist bearing a specific scaffold. Moreover, rational lead optimization requires rigorous
401 physical description of molecular recognition (Beuming and Shi, 2017), which depends on
402 adequate understanding of the conformational boundary and flexibility of the targeted state. We
403 have shown previously that both dopamine receptor subtype selectivity and modulation of agonist
404 efficacy can be achieved through the design of ligands that extend from the OBS into an
405 extracellular secondary binding pocket (SBP) (Michino et al., 2015a; Newman et al., 2012). We
406 now show that one might consider the occupation of the $Ile^{3.40}$ sub-pocket in the process of
407 decorating an D_2R antagonist scaffold to attain a desired level of inverse agonism. Our findings
408 also reveal allosteric communication between the $Ile^{3.40}$ sub-pocket and the Na^+ binding site. Thus,
409 Na^+ sensitivity in antagonist binding may provide useful mechanistic insights as part of such efforts.

410 The mutation of Trp100$^{EL1.50}$ in D_2R to alanine, leucine or phenylalanine cause substantial
411 increases in both the association and dissociation rate of risperidone (Wang et al., 2018).
412 Curiously, both the dissociation and association rates of D_2R antagonists used as antipsychotics
413 have been proposed to determine their propensity to cause extrapyramidal side-effects and
414 hyperprolactinaemia (Seeman, 2014; Sykes et al., 2017). Our results indicate that both the EL2
415 conformation and antagonist scaffolds may influence the dynamics of Trp100$^{EL1.50}$, which in turn
416 controls ligand access and egress to and from the OBS. Thus, understanding the relationship
417 between the distinct inactive D_2R conformations stabilized by different antagonist scaffolds and
418 these kinetic parameters will likely be important to facilitate the design of D_2R antagonists with an
419 optimal kinetic profile that minimizes the risk of side effects.

420 Previously, using the substituted-cysteine accessibility method (SCAM) in D_2R (Javitch et al.,
421 2000; Shi and Javitch, 2004), we found that G173$^{EL2.37}$C, N175 $^{EL2.39}$C, and I184$^{EL2.52}$C were
422 accessible to charged MTS reagents and that this accessibility could be blocked by the bound
423 Na^+-sensitive antagonist sulpiride, consistent with their water accessibility and involvement in
424 ligand binding and not with a static orientation facing lipid, whereas A177$^{EL2.45}$C and I183$^{EL2.51}$C
425 were accessible but not protected by sulpiride. Curiously, in the D_2R/risperidone structure,
426 Ile184$^{EL2.52}$ is only marginally in contact with the ligand, Ile183$^{EL2.51}$ blocks the accessibility of
427 Gly173$^{EL2.37}$ to the OBS and is itself buried in a hydrophobic pocket, whereas Asn175$^{EL2.39}$ faces
428 lipid, where it would be much less reactive. In the D_3R/eticlopride structure, Ile183$^{EL2.52}$ is in close
429 contact with the bound ligand, Ser182$^{EL2.51}$ faces the extracellular vestibule, whereas the
430 sidechain of Asn173$^{EL2.39}$ is oriented towards the OBS (Figure 5 – figure supplement 5). Thus, our
431 analysis shows that the accessibility pattern of EL2 revealed by previous SCAM studies in D_2R
432 are more consistent with the extended EL2 conformation revealed by the D_3R/eticlopride structure
433 but not with the D_2R/risperidone structure. Indeed, we observed spontaneous transitions of EL2
434 from a helical to extended conformation in our D_2R simulations, which suggests that EL2 of D_2R
435 exists in an ensemble of structured and unwound conformations, with substantial occupation of

436 the configuration found in the D_3R structure. Such dynamics of EL2 suggest that the drastically
437 different conformations between the D_2R and D_3R structures near EL2 are not related to the
438 divergence of the receptors. Thus, the D_2R EL2 appears to have quite dramatic dynamics that
439 are not captured by the crystal structure.

440 Taken together, our findings reveal that both the plasticity of the transmembrane domain in
441 accommodating different scaffolds and the dynamics of EL2 and EL1 are important considerations
442 in RDD targeting the inactive conformation of D_2R.

443 **METHODS**

444 **Key Resources Table**

Reagent type (species) or resource	Designation	Source or reference	Identifiers	Additional information
cell line (*Cricetulus griseus*)	FlpIn CHO	Invitrogen	Cat# R75807	
transfected construct (human)	SNAP-D_{2S}R	Cisbio	Cat# pSNAPD2	
transfected construct (human)	D_2R $G\alpha_{oA}$-RLuc8 Gβ1 Gγ2-Venus	Michino et al., 2017	N/A	
commercial assay or kit	Spiperone-d2 SNAP-Lumi4-Tb 5x SNAP/CLIP labelling medium	Cisbio	Cat# L0002RED Cat# SSNPTBX Cat# LABMED	
chemical compound, drug	Na bisulfite Glucose (+)-Butaclamol Risperidone Haloperidol	Sigma Aldrich	Cat# 243973 Cat# D9434 Cat# D033 Cat# R3030 Cat# H1512	
chemical compound, drug	Spiperone	Cayman chemicals	Cat# 19769	
chemical compound, drug	Eticlopride HCl Raclopride (-)-Sulpiride Quinpirole	Tocris Bioscience	Cat# 1847 Cat# 1810 Cat# 0895 Cat# 1061	
chemical compound, drug	[^{3}H]spiperone	Perkin Elmer	Cat# NET1187250UC	
chemical compound, drug	Polyethylenimine	Polysciences	Cat# 23966	
chemical compound, drug	Coelenterazine-h	NanoLight Technology	Cat# 301-5	
software, algorithm	Prism	GraphPad	v7.0 and v8.2.1	

445 **Residue indices in EL1 and EL2**

446 Based on a systematic analysis of aminergic receptors, we found a Trp in the middle of EL1
447 and the disulfide-bonded Cys in the middle of EL2 are the most conserved residues in each
448 segment, and defined their residue indices as EL1.50 and EL2.50, respectively (Michino et al.,
449 2015a), In this study, for the convenience of comparisons among D_2R, D_3R, and D_4R, and 5-
450 $HT_{2A}R$, based on the alignments of EL1 And EL2 shown in Figure 5 – figure supplement 1, we
451 index the EL1 and EL2 residues of each receptor in the same way as the Ballesteros-Weinstein
452 numbering, e.g., the residues before and after the EL2.50 are EL2.49 and EL2.51, respectively.
453 Note the indices for the shorter sequences are not be consecutive, given the gaps in the alignment.

454 **Molecular modeling and docking**

455 The D_2R models in this study are based on the corrected crystal structure of D_2R bound to
456 risperidone (PDB: 6CM4) (Wang et al., 2018). We omitted T4 Lysozyme fused into intracellular
457 loop 3. Three thermostabilizing mutations (Ile122$^{3.40}$A, L375$^{6.37}$A, and L379$^{6.41}$A) were reverted to
458 their WT residues. The missing N terminus in the crystal structure was built de novo using Rosetta
459 (Bradley et al., 2005), and then integrated with the rest of the D_2R model using Modeller (John
460 and Sali, 2003). Using Modeller, we also extended two helical turns at the TM5 C terminus and
461 threes residues at the TM6 N terminus of the structure and connected these two ends with a 9
462 Gly loop, similar to our experimentally validated treatment of D3R models (Michino et al., 2017).
463 The position of the Na^+ bound in the canonical Na^+ binding site near the negatively charged Asp$^{2.50}$
464 was acquired by superimposing the Na^+ bound structure of adenosine A_{2A} receptor (Liu et al.,
465 2012) to our D_2R models.

466 The binding poses of risperidone and eticlopride were taken according to their poses in the
467 D_2R (Wang et al., 2018) and D_3R (Chien et al., 2010) structures, respectively. Docking of
468 spiperone in our D2R model was performed using the induced-fit docking (IFD) protocol (Sherman
469 et al., 2006) in the Schrodinger software (release 2017-2; Schrodinger, LLC: New York NY).

470 Based on our hypothesis regarding the role of the $Ile^{3.40}$ sub-pocket in the Na^+ sensitivity (see
471 text), from the resulting poses of IFD, we choose the spiperone pose with the F-substitution on
472 the butyrophenone ring occupying the $Ile^{3.40}$ sub-pocket. Note that in risperidone and spiperone
473 the F-substitutions have similar distances to the protonated N atoms that interact with $Asp^{3.32}$
474 (measured by the number of carbon atoms between them, Figure 1 – figure supplement 1).

475 **Molecular dynamics (MD) simulations**

476 MD simulations of the D_2R and D_3R complexes were performed in the explicit water and 1-
477 palmitoyl-2-oleoylphosphatidylcholine (POPC) lipid bilayer environment using Desmond MD
478 System (version 4.5; D. E. Shaw Research, New York, NY) with either the OPLS3e force field
479 (Roos et al., 2019) or the CHARMM36 force field (Best et al., 2012; Klauda et al., 2010; MacKerell
480 et al., 1998; MacKerell et al., 2004) and TIP3P water model. For CHARMM36 runs, the eticlopride
481 parameters were obtained through the GAAMP server (Huang and Roux, 2013), with the initial
482 force field based on CGenFF assigned by ParamChem (Vanommeslaeghe et al., 2010). The
483 system charges were neutralized, and 150 mM NaCl was added. Each system was first minimized
484 and then equilibrated with restraints on the ligand heavy atoms and protein backbone atoms,
485 followed by production runs in an isothermal–isobaric (NPT) ensemble at 310 K and 1 atom with
486 all atoms unrestrained, as described previously (Michino et al., 2017; Michino et al., 2015b). We
487 used Langevin constant pressure and temperature dynamical system (Feller et al., 1995) to
488 maintain the pressure and the temperature, on an anisotropic flexible periodic cell with a constant-
489 ratio constraint applied on the lipid bilayer in the X-Y plane. For each condition, we collected
490 multiple trajectories, the aggregated simulation length is ~392 μs (Table 1).

491 While the majority of our D_2R simulations in this study used the OPLS3 force field, to compare
492 with the D_3R simulations using CHARMM36 that have been continued from the previously
493 reported shorter trajectories (Michino et al., 2017; Michino et al., 2015b), we carried out the
494 D_2R/eticlopride simulations using both the OPLS3 and CHARMM36 force fields (see Table 1). We

495 did not observe significant differences and pooled their results together for the analysis.

496 **Conformational analysis**

497 Distances and dihedral angles of MD simulation results were calculated with MDTraj (version
498 1.8.2) (McGibbon et al., 2015) in combination with *in-house* Python scripts.

499 To characterize the structural changes in the receptor upon ligand binding, we quantified
500 differences of structural elements between the D_2R/eticlopride and D_2R/risperidone conditions
501 (using last 600 ns from a representative trajectory for each condition), by applying the previously
502 described pairwise interaction analyzer for GPCR (PIA-GPCR) (Michino et al., 2017). The
503 subsegments on the extracellular side of D_2R were defined as following: TM1e (the extracellular
504 subsegment (e) of TM1, residues 31-38), TM2e (residues 92-96), TM3e (residues 104-113),
505 TM4e (residues 166-172), TM5e (residues 187-195), TM6e (residues 364-369), and TM7e
506 (residues 376-382).

507 For the PIA-GPCR analysis in Figure 4 and the distance analysis in Figure 6, we used the set
508 of ligand binding residues previously identified by our systematic analysis of GPCR structures.
509 Specifically, for D_2R, they are residues 91, 94, 95, 100, 110, 111, 114, 115, 118, 119, 122, 167,
510 184, 189, 190, 193, 194, 197, 198, 353, 357, 360, 361, 364, 365, 367, 368, 376, 379, 380, 383,
511 384, 386, and 387; for D_3R, they are residues 86, 89, 90, 96, 106, 107, 110, 111, 114, 115, 118,
512 165, 183, 188, 189, 192, 193, 196, 197, 338, 342, 345, 346, 349, 350, 352, 353, 362, 365, 366,
513 369, 370, 372, and 373.

514 For the clustering of the OBS conformations, we used representative D_2R/eticlopride and
515 D_2R/risperidone MD trajectories in which EL2 transitioned from the helical to unwound
516 conformations. For each complex, using the Ile183-Asn186 distance as a criterion to differentiate
517 the EL2 conformation (Figure 5), 1000 MD frames with helical EL2 conformations and another
518 1000 frames with extended EL2 conformations were randomly selected. For these 4000 frames,
519 the pair RMSD of the backbone heavy atoms of the OBS residues defined in (Michino et al.,

520 2015a), except for Ile184$^{EL2.50}$, were calculated. The resulting 4000x4000 matrix was used to
521 cluster these frames using the k-mean algorithm implemented in R. We chose nstart to be 20 to
522 assure the convergence of cluster centroids and boundaries. We chose the clustering level to be
523 4, so that the average pairwise RMSDs (apRMSDs) between the D_2R/eticlopride and
524 D_2R/risperidone clusters are similar to that between D_2R and D_3R structures (1.2 Å), while all the
525 apRMSDs within a cluster are smaller than those between any given two clusters. The same
526 frame selection and clustering procedure was repeated to 20 times. The average of these 20 runs
527 were reported in Table 4.

528 **Markov State Model (MSM) analysis**

529 The MSM analysis was performed using the pyEMMA program (version 2.5.5) (Scherer et al.,
530 2015). To characterize the dynamics of EL2 of D_2R, specifically the transitions between helical
531 and extended conformations of its C-terminal portion, we focused on a key hydrogen bond formed
532 in the helical conformation between the backbone carbonyl group of Ile183 and the backbone
533 amine group of Asn186. Thus, for each of the simulated conditions, the distance of Ile183-Asn186
534 (Ser182-Asn185 in D_3R) was used as an input feature for the MSM analysis. We discretized this
535 feature into two clusters – distances below and above 4 Å (i.e. EL2 forming a helical conformation
536 and unwinding). Implied relaxation timescale (ITS) (Swope et al., 2004) for the transition between
537 these clusters was obtained as a function of various lag times. Convergences of ITS for the MSMs
538 for all conditions was achieved at a lag time of 300 ns (Figure 5 – figure supplement 6), which we
539 further used to estimate Bayesian Markov models with 500 transition matrix samples
540 (Trendelkamp-Schroer and Noe, 2013). The maximum likelihood transition matrix was used to
541 calculate the transition and equilibrium probabilities (π) shown in Figure 5 and Figure 5 – figure
542 supplement 3.

543 **Cell culture and cell line generation**

544 Site directed mutagenesis was performed using the Quickchange method using

545 pEF5/DEST/FRT plasmid encoding FLAG-SNAP-D_{2S}R as the DNA template. The mutagenesis
546 was confirmed, and the full coding region was checked using Sanger sequencing at the DNA
547 Sequencing Laboratory (University of Nottingham). Stable cell lines were generated using the Flp-
548 In™ recombination system (Invitrogen).

549 **[^{3}H]spiperone binding assay**

550 FlpIn CHO cells (Invitrogen) stably expressing WT or mutant SNAP-D2s cells were cultured
551 before the preparation of cell membrane as described before (Klein Herenbrink et al., 2019).
552 All stable cell lines were confirmed to be mycoplasma free. For saturating binding assays cell
553 membranes (Mutant or WT SNAP-D_{2s}-FlpIn CHO, 2.5 µg) were incubated with varying
554 concentrations of [^{3}H]spiperone and 10 µM haloperidol as a non-specific control, in binding
555 buffer (20 mM HEPES, 100 mM NaCl, 6 mM $MgCl_2$, 1mM EGTA, and 1mM EDTA, pH 7.4) to
556 a final volume of 200 µL and were incubated at 37 °C for 3 h. For competition binding assays
557 cell membranes (SNAP-D_{2s}-FlpIn CHO, 2.5 µg) were incubated with varying concentrations of
558 test compound in binding buffer containing 0.2 nM of [^{3}H]spiperone to a final volume of 200 µL
559 and were incubated at 37 °C for 3 h. Binding was terminated by fast-flow filtration using a
560 Uniplate 96-well harvester (PerkinElmer) followed by five washes with ice-cold 0.9% NaCl.
561 Bound radioactivity was measured in a MicroBeta2 LumiJET MicroBeta counter (PerkinElmer).
562 Data were collected from at least 3 separate experiments performed in triplicate and analysed
563 using non-linear regression (Prism 7, Graphpad software). For radioligand saturation binding
564 data, the following equation was globally fitted to nonspecific and total binding data:

565

566 $$Y = \frac{B_{\max}[A]}{[A]+K_A} + NS[A] \quad (1)$$

567 Where Y is radioligand binding, B_{max} is the total receptor density, [A] is the free radioligand
568 concentration, K_A is the equilibrium dissociation constant of the radioligand, and NS is the
569 fraction of nonspecific radioligand binding. The B_{max} of the SNAP-tagged D2SRs we as follows;

570 WT = 7.95 ± 1.63 pmol.mg^{-1}, 6.39 ± 1.04 pmol.mg^{-1}, 4.37 ± 0.92 pmol.mg^{-1}, 2.61 ± 0.50 pmol.mg^{-}
571 ^{1}.

572 For competition binding assays, the concentration of ligand that inhibited half of the
573 [^{3}H]spiperone binding (IC_{50}) was determined by fitting the data to the following equation:

574 $$Y = \frac{Bottom+(Top-Bottom)}{1+10^{(X-LogIC_{50})n_H}} \quad (2)$$

575 Where Y denotes the percentage specific binding, Top and Bottom denote the maximal and
576 minimal asymptotes, respectively, IC_{50} denotes the X-value when the response is midway
577 between Bottom and Top, and *n*H denotes the Hill slope factor. IC_{50} values obtained from the
578 inhibition curves were converted to K_i values using the Cheng and Prusoff equation. No
579 statistical methods were used to predetermine sample size.

580 **Bioluminescence resonance energy transfer (BRET) assay**

581 The Go-protein activation assay uses a set of BRET-based constructs previously described
582 (Michino et al., 2017). Briefly, HEK293T cells were transiently co-transfected with pcDNA3.1
583 vectors encoding i) D_2R, ii) $G\alpha_{oA}$ fused to Renilla luciferase 8 (Rluc8; provided by Dr. S. Gambhir,
584 Stanford University, Stanford, CA) at residue 91, iii) untagged Gβ1, and iv. Gγ2 fused to mVenus.
585 Transfections were performed using polyethyleneimine (PEI) at a ratio of 2:1 (PEI:total DNA;
586 weight:weight), and cell culture was maintained as described previously (Bonifazi et al., 2019).
587 After ~48 h of transfection, cells were washed with PBS and resuspended in PBS + 0.1% glucose
588 + 200 μM Na Bisulfite buffer. Approximately 200,000 cells were then distributed in each well of
589 the 96-well plates (White Lumitrac 200, Greiner bio-one). 5 μM Coelenterazine H, a luciferase
590 substrate for BRET, was then added followed by addition of vehicle and test compounds using an
591 automated stamp transfer protocol (Nimbus, Hamilton Robotics) from an aliquoted 96-well
592 compound plate. Following ligands were used – quinpirole, eticlopride, raclopride, and (-)-sulpiride
593 (Tocris Bioscience), (+)-butaclamol, dopamine, and risperidone (Sigma Aldrich), and Spiperone
594 (Cayman chemicals). mVenus emission (530 nm) over RLuc 8 emission (485 nm) were then

595 measured after 30 min of ligand incubation at 37°C using a PHERAstar *FSX* plate reader (BMG
596 Labtech). BRET ratio was then determined by calculating the ratio of mVenus emission over RLuc
597 8 emission.
598 Data were collected from at least 9 independent experiments and analyzed using Prism 7
599 (GraphPad Software). Drug-induced BRET, defined by BRET ratio difference in the presence and
600 absence of compounds, was calculated. Concentration response curves (CRCs) were generated
601 using a non-linear sigmoidal dose-response analyses using Prism 7 (GraphPad Software). CRCs
602 are presented as mean drug-induced BRET ± SEM. E_{max} bar graphs are plotted as the percentage
603 of maximal drug-induced BRET by (+)-Butaclamol ± SEM.

604 **Tr-FRET ligand binding**

605 *Materials:* Spiperone-d2, SNAP-Lumi4-Tb and 5x SNAP/CLIP labelling medium were purchased
606 from Cisbio Bioassays. Eticlopride hydrochloride was purchased from Tocris Bioscience. Saponin
607 was purchased from Fluka/Sigma-Aldrich. Bromocriptine, haloperidol, risperidone, spiperone,
608 pluronic-F127, Gpp(NH)p, DNA primers, Hanks Balanced Salt Solution H8264 (HBSS) and
609 phosphate buffered saline (PBS) was purchased from Sigma-Aldrich.
610 *Terbium cryptate labelling and membrane preparation:* Terbium cryptate labelling of the SNAP-
611 tagged receptors and membrane preparation was performed with minor changes to previously
612 described methods (Klein Herenbrink et al., 2016). Flp-In CHO-K1 cells stably expressing the
613 mutant SNAP-D_{2S}R constructs were grown in T175 flasks to approximately 90% confluency. Cell
614 media was aspirated, and the cells were washed twice with 12mL PBS. The cells were then
615 incubated with terbium cryptate labelling reagent in 1xSNAP/CLIP labelling medium for one hour
616 at in a humidified cell culture incubator with 5% CO_2 at 37°C. The terbium cryptate labelling
617 reagent was then removed and the cells were washed once with 12mL PBS. The labelled cells
618 were then harvested in 10mL PBS by cell scraping. Harvested cells were then collected by
619 centrifugation at 300g for 5 minutes and removal of the supernatant. The cell pellets were then

620 frozen at -80°C for later membrane preparation. For cell membrane preparation, each cell pellet
621 was removed from the -80°C freezer and thawed on ice. The pellet was then resuspended in
622 10mL of ice-cold Buffer 1 (10mM HEPES 10mM EDTA pH7.4). The pellet was then homogenised
623 (IKA works T 10 basic Ultra-Turrax® homogeniser) with eight bursts of three seconds on setting
624 4. The homogenised cells were transferred to an ultra-fast centrifuge tube and an additional 10mL
625 of Buffer 1 was added. The tube was then centrifuged at 48,000g for 30 minutes at 4°C. The
626 supernatant was discarded, 20mL of Buffer 1 was added and the pellet was resuspended. The
627 resuspension was then centrifuged a second time at 48,000g for 30 minutes at 4°C. The
628 supernatant was then removed, and the cell membrane pellet was collected by resuspension in
629 2mL ice-cold Buffer 2 (10mM HEPES 0.1mM EDTA pH 7.4). The resuspended membranes were
630 then put through a syringe with a BD precision glide 26-gauge needle to make the solution uniform.
631 Membrane protein concentration was determined by bicinchonic acid (BCA) assay detecting the
632 absorbance at 562nm on a CLARIOstar plate reader (BMG Labtech) using bovine serum albumin
633 (BSA) as the protein standard. The cell membrane solution was then aliquoted and frozen at -
634 80°C.
635 *TR-FRET binding assay*: All ligands were diluted in Binding Buffer (Hanks Balanced Salt Solution
636 (Sigma H8264), 20mM HEPES, 0.02% Pluronic-F127, 1% dimethyl sulfoxide, pH 7.4 (with KOH)).
637 For competition kinetic binding experiments; 10µL of spiperone-d2 in Binding Buffer was added
638 to each well of a 384-well white optiplate LBS coated (PerkinElmer) at varied concentrations
639 depending on the SNAP-D_{2S}R mutant. 10µL of increasing concentrations of unlabelled ligands
640 were then added into the 10µL of fluorescent ligand and mixed. A final concentration of 100µM
641 haloperidol was used to determine non-specific binding. Cell membranes were diluted to
642 0.075µg/µL in Binding Buffer supplemented with 50µg/mL saponin and 100µM Gpp(NH)p.
643 TR-FRET measurements were acquired on a PHERAstar *FS* plate reader (BMG Labtech) at
644 37°C. The optiplate containing the ligand cocktails in the wells was incubated in the instrument
645 for 6 minutes. The cell membrane solution was primed into the on-board injection system and

646 incubated for 5 minutes. 20µL of cell membrane solution was injected at 400µL/s into the ligand
647 cocktail wells to initiate the binding reaction. After 30 minutes incubation, the HTRF optic filter
648 module was used to perform an excitation at 337nm and simultaneous dual emission detection at
649 620nm (terbium cryptate donor) and 665nm (fluorescent ligand acceptor). The focal height was
650 set to 10.4mm. All experiments were performed in singlet wells. The TR-FRET binding values
651 were determined by dividing the by the fluorescent ligand acceptor channel values by the terbium
652 cryptate donor channel values and multiplying by 10,000. These values were then subtracted by
653 the non-specific binding values determined in each experiment to give the specific HTRF ratio x
654 10,000. The data was then analysed with GraphPad Prism 8.2.1 using equations 1 and 2.
655

656 **Acknowledgements**

657 Support for this research was provided by the National Institute on Drug Abuse–Intramural
658 Research Program, Z1A DA000606-03 (L.S.), NIH grant MH54137 (J.A.J.) and National Health
659 and Medical Research Council (NHMRC) Project Grant APP1049564 (J.R.L). We thank Jackie
660 Glenn for technical support in generating membrane preparations.

661

662 **Competing financial interests**

663 The authors declare no competing financial interests.

664 **TABLES**

665 **Table 1.** Summary of molecular dynamics simulations.

receptor	ligand	bound Na^+	number of OPLS3 trajectories	Number of CHARMM36 trajectories	accumulated simulation time (ns)
D_2R	risperidone	+	12		28410
		-	11		42240
	spiperone	+	22		42000
		-	17		29550
	eticlopride	+	5	12	51540
		-	7		11280
	(-)-sulpiride	+	3		4500
		-	3		3600
	aripiprazole	+	40		66660
D_3R	eticlopride	+		3	13200
		-		4	6240
	R22	+		7	33600
	S22	-		7	59400
Total			120	33	392220

666 **Table 2**. The effect of mutations on the binding affinities of selected D_2R ligands. The affinities of
667 [^{3}H]spiperone were determined in saturation experiments at WT or mutant SNAP-tagged D_{2S}Rs
668 stably expressed in FlpIn CHO cells. Binding affinity values for risperidone and eticlopride were
669 obtained in competition binding experiments. Means of n independent experiments performed in
670 triplicate are shown with 95% confidence intervals.

	[^{3}H]spiperone saturation binding		[^{3}H]spiperone competition binding			
SNAP-D_{2S}R	pK_d (K_d, nM) (95% CI)	n	Risperidone pK_i (K_i, nM) (95% CI)	n	Eticlopride pK_i (K_i, nM) (95% CI)	n
WT	9.74 (0.18) (9.36 – 10.14)	3	8.55 (2.8) (8.07 – 9.04)	8	9.84 (0.14) (9.10 - 10.58)	3
WT -Na^+	9.70 (0.20) (9.09 – 10.32)	3	8.96 (1.1) (8.84 – 9.08)	6	-	
I122$^{3.40}$A	9.74 (0.18) (9.09 – 10.38)	3	8.14 (7.9) (7.97 – 8.32)	8	10.33 (0.04) (10.22 – 10.44)	3
I122$^{3.40}$W	8.95 (1.15) (8.59 – 9.30)	3	7.43 (37) (7.11 – 7.75)	5	9.61 (0.25) (9.33 – 9.89)	4

671 **Table 3**. The effect of mutations on the binding affinities of selected D_2R ligands as determined in Tr-FRET binding experiments. The
672 affinities of the fluorescently labelled spiperone derivative (Spiperone-d2) or unlabelled antagonists were determined in saturation
673 experiments at WT or mutant SNAP-tagged $D_{2S}Rs$ stably expressed in FlpIn CHO cells. Binding affinity values for risperidone and
674 eticlopride were obtained in competition binding experiments. Means of n independent experiments are shown with 95% confidence
675 intervals (CIs). * = significantly different from WT value, $P < 0.05$, one-way ANOVA with Dunnett's post-hoc test

	Spiperone-d2 saturation binding			Spiperone-d2 Competition binding								
SNAP-$D_{2S}R$	pK_d (K_d, nM) (95% CI)	n	Mut/WT	Eticlopride pK_i (K_i, nM) (95% CI)	n	Mut/WT	Risperidone pK_i (K_i, nM) (95% CI)	n	Mut/WT	Spiperone pK_i (K_i, nM) (95% CI)	n	Mut/WT
WT	8.54 (2.88) (8.32 – 8.77)	9	1.0	10.06 (0.09) (9.90 – 10.21)	8	1.0	8.47 (3.34) (8.15 – 8.80)	7	1.0	9.96 (0.11) (9.76 – 10.18)	8	1.0
L94A	7.71 (19.5) (7.41 – 8.00)*	5	6.8	9.08 (0.83) (8.91 – 9.08)*	4	9.2	8.02 (9.54) (7.86 – 8.17)*	5	2.9	8.36 (4.37) (8.21 – 8.50)*	5	39.7
W100A	7.39 (40.7) (7.21 – 7.56)*	9	14.1	8.06 (8.71) (7.78 – 8.32)*	4	96.8	7.60 (25.1) (7.41 – 7.79)*	7	7.5	8.39 (4.07) (8.19 – 8.59)*	7	37.0
I184A	8.79 (1.62) (8.58 – 9.00)	5	0.6	9.34 (0.45) (8.94 – 9.75)*	4	5	9.33 (0.47) (9.18 – 9.48)*	5	0.1	9.78 (0.17) (9.51 – 10.05)	5	1.6

676 **Table 4.** Clustering results of the OBS conformations sampled in the D_2R/eticlopride and
677 D_2R/risperidone simulations. The compositions in each cluster are shown as percentages of the
678 frames randomly extracted for each complex (see Methods), when sorted by either
679 receptor/ligand complex or EL2 conformation.

cluster ID	percentage (%)							
	complex				EL2 conformation			
	D_2R/eticlopride		D_2R/risperidone		extended		helical	
	mean	sd	mean	sd	mean	sd	mean	sd
1	38.4	0.7	0.0	0.0	4.9	0.4	33.5	0.5
2	61.6	0.7	0.0	0.0	45.1	0.4	16.5	0.6
3	0.0	0.0	43.7	1.0	2.5	0.4	41.3	0.8
4	0.0	0.0	56.3	1.0	47.5	0.4	8.7	0.8

680 **REFERENCES**

681 Abramyan, A.M., Quick, M., Xue, C., Javitch, J.A., and Shi, L. (2018). Exploring Substrate Binding
682 in the Extracellular Vestibule of MhsT by Atomistic Simulations and Markov Models. Journal of
683 chemical information and modeling *58*, 1244-1252.

684 Amaro, R.E., Baudry, J., Chodera, J., Demir, O., McCammon, J.A., Miao, Y., and Smith, J.C.
685 (2018). Ensemble Docking in Drug Discovery. Biophys J *114*, 2271-2278.

686 Ballesteros, J., and Weinstein, H. (1995). Integrated methods for the construction of three-
687 dimensional models of structure-function relations in G protein-coupled receptors. Methods in
688 Neurosciences *25*, 366-428.

689 Best, R.B., Zhu, X., Shim, J., Lopes, P.E., Mittal, J., Feig, M., and Mackerell, A.D., Jr. (2012).
690 Optimization of the additive CHARMM all-atom protein force field targeting improved sampling
691 of the backbone phi, psi and side-chain chi(1) and chi(2) dihedral angles. J Chem Theory
692 Comput *8*, 3257-3273.

693 Beuming, T., and Shi, L. (2017). Editorial: Computer Aided Structure-based Lead Optimization.
694 Curr Top Med Chem *17*, 2575-2576.

695 Bonifazi, A., Yano, H., Guerrero, A.M., Kumar, V., Hoffman, A.F., Lupica, C.R., Shi, L., and
696 Newman, A.H. (2019). Novel and Potent Dopamine D2 Receptor Go-Protein Biased Agonists.
697 ACS Pharmacol Transl Sci *2*, 52-65.

698 Bradley, P., Misura, K.M., and Baker, D. (2005). Toward high-resolution de novo structure
699 prediction for small proteins. Science *309*, 1868-1871.

700 Chien, E.Y., Liu, W., Zhao, Q., Katritch, V., Han, G.W., Hanson, M.A., Shi, L., Newman, A.H.,
701 Javitch, J.A., Cherezov, V.*, et al.* (2010). Structure of the human dopamine D3 receptor in
702 complex with a D2/D3 selective antagonist. Science *330*, 1091-1095.

703 Congreve, M., Dias, J.M., and Marshall, F.H. (2014). Structure-based drug design for G protein-
704 coupled receptors. Prog Med Chem *53*, 1-63.

705 Feller, S.E., Zhang, Y., Pastor, R.W., and Brooks, B.R. (1995). Constant pressure molecular

706 dynamics simulation: The Langevin piston method. J Chem Phys *103*, 4613-4621.
707 Free, R.B., Chun, L.S., Moritz, A.E., Miller, B.N., Doyle, T.B., Conroy, J.L., Padron, A., Meade,
708 J.A., Xiao, J., Hu, X.*, et al.* (2014). Discovery and characterization of a G protein-biased agonist
709 that inhibits beta-arrestin recruitment to the D2 dopamine receptor. Mol Pharmacol *86*, 96-105.
710 Hirose, T., and Kikuchi, T. (2005). Aripiprazole, a novel antipsychotic agent: dopamine D2
711 receptor partial agonist. J Med Invest *52 Suppl*, 284-290.
712 Huang, L., and Roux, B. (2013). Automated Force Field Parameterization for Non-Polarizable and
713 Polarizable Atomic Models Based on Ab Initio Target Data. J Chem Theory Comput *9*.
714 Ioerger, T.R., Du, C., and Linthicum, D.S. (1999). Conservation of cys-cys trp structural triads and
715 their geometry in the protein domains of immunoglobulin superfamily members. Mol Immunol
716 *36*, 373-386.
717 Javitch, J.A., Shi, L., Simpson, M.M., Chen, J., Chiappa, V., Visiers, I., Weinstein, H., and
718 Ballesteros, J.A. (2000). The fourth transmembrane segment of the dopamine D2 receptor:
719 accessibility in the binding-site crevice and position in the transmembrane bundle. Biochemistry
720 *39*, 12190-12199.
721 John, B., and Sali, A. (2003). Comparative protein structure modeling by iterative alignment,
722 model building and model assessment. Nucleic Acids Res *31*, 3982-3992.
723 Kimura, K.T., Asada, H., Inoue, A., Kadji, F.M.N., Im, D., Mori, C., Arakawa, T., Hirata, K., Nomura,
724 Y., Nomura, N.*, et al.* (2019). Structures of the 5-HT2A receptor in complex with the
725 antipsychotics risperidone and zotepine. Nat Struct Mol Biol *26*, 121-128.
726 Klauda, J.B., Venable, R.M., Freites, J.A., O'Connor, J.W., Tobias, D.J., Mondragon-Ramirez, C.,
727 Vorobyov, I., MacKerell, A.D., Jr., and Pastor, R.W. (2010). Update of the CHARMM all-atom
728 additive force field for lipids: validation on six lipid types. J Phys Chem B *114*, 7830-7843.
729 Klein Herenbrink, C., Sykes, D.A., Donthamsetti, P., Canals, M., Coudrat, T., Shonberg, J.,
730 Scammells, P.J., Capuano, B., Sexton, P.M., Charlton, S.J.*, et al.* (2016). The role of kinetic
731 context in apparent biased agonism at GPCRs. Nat Commun *7*, 10842.

732 Klein Herenbrink, C., Verma, R., Lim, H.D., Kopinathan, A., Keen, A., Shonberg, J., Draper-Joyce,
733 C.J., Scammells, P.J., Christopoulos, A., Javitch, J.A.*, et al.* (2019). Molecular Determinants of
734 the Intrinsic Efficacy of the Antipsychotic Aripiprazole. ACS Chem Biol *14*, 1780-1792.
735 Latorraca, N.R., Venkatakrishnan, A.J., and Dror, R.O. (2017). GPCR Dynamics: Structures in
736 Motion. Chem Rev *117*, 139-155.
737 Liu, W., Chun, E., Thompson, A.A., Chubukov, P., Xu, F., Katritch, V., Han, G.W., Roth, C.B.,
738 Heitman, L.H., AP, I.J.*, et al.* (2012). Structural basis for allosteric regulation of GPCRs by
739 sodium ions. Science *337*, 232-236.
740 MacKerell, A.D., Bashford, D., Bellott, Dunbrack, R.L., Evanseck, J.D., Field, M.J., Fischer, S.,
741 Gao, J., Guo, H., Ha, S.*, et al.* (1998). All-Atom Empirical Potential for Molecular Modeling and
742 Dynamics Studies of Proteins†. J Phys Chem B *102*, 3586-3616.
743 MacKerell, A.D., Jr., Feig, M., and Brooks, C.L., 3rd (2004). Improved treatment of the protein
744 backbone in empirical force fields. J Am Chem Soc *126*, 698-699.
745 Malinauskaite, L., Quick, M., Reinhard, L., Lyons, J.A., Yano, H., Javitch, J.A., and Nissen, P.
746 (2014). A mechanism for intracellular release of Na+ by neurotransmitter/sodium symporters.
747 Nat Struct Mol Biol *21*, 1006-1012.
748 Manglik, A., Lin, H., Aryal, D.K., McCorvy, J.D., Dengler, D., Corder, G., Levit, A., Kling, R.C.,
749 Bernat, V., Hubner, H.*, et al.* (2016). Structure-based discovery of opioid analgesics with
750 reduced side effects. Nature *537*, 185-190.
751 McCorvy, J.D., Butler, K.V., Kelly, B., Rechsteiner, K., Karpiak, J., Betz, R.M., Kormos, B.L.,
752 Shoichet, B.K., Dror, R.O., Jin, J.*, et al.* (2018). Structure-inspired design of beta-arrestin-biased
753 ligands for aminergic GPCRs. Nature chemical biology *14*, 126-134.
754 McGibbon, R.T., Beauchamp, K.A., Harrigan, M.P., Klein, C., Swails, J.M., Hernandez, C.X.,
755 Schwantes, C.R., Wang, L.P., Lane, T.J., and Pande, V.S. (2015). MDTraj: A Modern Open
756 Library for the Analysis of Molecular Dynamics Trajectories. Biophys J *109*, 1528-1532.
757 Michino, M., Beuming, T., Donthamsetti, P., Newman, A.H., Javitch, J.A., and Shi, L. (2015a).

758 What can crystal structures of aminergic receptors tell us about designing subtype-selective
759 ligands? Pharmacol Rev *67*, 198-213.
760 Michino, M., Boateng, C.A., Donthamsetti, P., Yano, H., Bakare, O.M., Bonifazi, A., Ellenberger,
761 M.P., Keck, T.M., Kumar, V., Zhu, C.*, et al.* (2017). Toward Understanding the Structural Basis
762 of Partial Agonism at the Dopamine D3 Receptor. J Med Chem *60*, 580-593.
763 Michino, M., Donthamsetti, P., Beuming, T., Banala, A., Duan, L., Roux, T., Han, Y., Trinquet, E.,
764 Newman, A.H., Javitch, J.A.*, et al.* (2013). A single glycine in extracellular loop 1 is the critical
765 determinant for pharmacological specificity of dopamine D2 and D3 receptors. Mol Pharmacol
766 *84*, 854-864.
767 Michino, M., Free, R.B., Doyle, T.B., Sibley, D.R., and Shi, L. (2015b). Structural basis for Na(+)-
768 sensitivity in dopamine D2 and D3 receptors. Chem Commun (Camb) *51*, 8618-8621.
769 Neve, K.A. (1991). Regulation of dopamine D2 receptors by sodium and pH. Mol Pharmacol *39*,
770 570-578.
771 Newman, A.H., Beuming, T., Banala, A.K., Donthamsetti, P., Pongetti, K., LaBounty, A., Levy, B.,
772 Cao, J., Michino, M., Luedtke, R.R.*, et al.* (2012). Molecular determinants of selectivity and
773 efficacy at the dopamine D3 receptor. J Med Chem *55*, 6689-6699.
774 Newton, C.L., Wood, M.D., and Strange, P.G. (2016). Examining the Effects of Sodium Ions on
775 the Binding of Antagonists to Dopamine D2 and D3 Receptors. PLoS One *11*, e0158808.
776 Piana, S., Lindorff-Larsen, K., and Shaw, D.E. (2011). How robust are protein folding simulations
777 with respect to force field parameterization? Biophys J *100*, L47-49.
778 Rasmussen, S.G., Choi, H.J., Fung, J.J., Pardon, E., Casarosa, P., Chae, P.S., Devree, B.T.,
779 Rosenbaum, D.M., Thian, F.S., Kobilka, T.S.*, et al.* (2011). Structure of a nanobody-stabilized
780 active state of the beta(2) adrenoceptor. Nature *469*, 175-180.
781 Roberts, D.J., and Strange, P.G. (2005). Mechanisms of inverse agonist action at D2 dopamine
782 receptors. Br J Pharmacol *145*, 34-42.
783 Roos, K., Wu, C., Damm, W., Reboul, M., Stevenson, J.M., Lu, C., Dahlgren, M.K., Mondal, S.,

784 Chen, W., Wang, L.*, et al.* (2019). OPLS3e: Extending Force Field Coverage for Drug-Like Small
785 Molecules. J Chem Theory Comput *15*, 1863-1874.
786 Roth, B.L., Lopez, E., Patel, S., and Kroeze, W.K. (2000). The Multiplicity of Serotonin Receptors:
787 Uselessly Diverse Molecules or an Embarrassment of Riches? The Neuroscientist *6*, 252-262.
788 Scherer, M.K., Trendelkamp-Schroer, B., Paul, F., Perez-Hernandez, G., Hoffmann, M., Plattner,
789 N., Wehmeyer, C., Prinz, J.H., and Noe, F. (2015). PyEMMA 2: A Software Package for
790 Estimation, Validation, and Analysis of Markov Models. J Chem Theory Comput *11*, 5525-5542.
791 Seeman, P. (2014). Clozapine, a fast-off-D2 antipsychotic. ACS chemical neuroscience *5*, 24-29.
792 Sherman, W., Day, T., Jacobson, M.P., Friesner, R.A., and Farid, R. (2006). Novel procedure for
793 modeling ligand/receptor induced fit effects. J Med Chem *49*, 534-553.
794 Shi, L., and Javitch, J.A. (2004). The second extracellular loop of the dopamine D2 receptor lines
795 the binding-site crevice. Proc Natl Acad Sci U S A *101*, 440-445.
796 Sibley, D.R., and Shi, L. (2018). A new era of rationally designed antipsychotics. Nature *555*, 170-
797 172.
798 Silvestre, J.S., and Prous, J. (2005). Research on adverse drug events. I. Muscarinic M3 receptor
799 binding affinity could predict the risk of antipsychotics to induce type 2 diabetes. Methods Find
800 Exp Clin Pharmacol *27*, 289-304.
801 Stolzenberg, S., Li, Z., Quick, M., Malinauskaite, L., Nissen, P., Weinstein, H., Javitch, J.A., and
802 Shi, L. (2017). The role of transmembrane segment 5 (TM5) in Na2 release and the
803 conformational transition of neurotransmitter:sodium symporters toward the inward-open state.
804 J Biol Chem *292*, 7372-7384.
805 Swope, W.C., Pitera, J.W., and Suits, F. (2004). Describing Protein Folding Kinetics by Molecular
806 Dynamics Simulations. 1. Theory†. The Journal of Physical Chemistry B *108*, 6571-6581.
807 Sykes, D.A., Moore, H., Stott, L., Holliday, N., Javitch, J.A., Lane, J.R., and Charlton, S.J. (2017).
808 Extrapyramidal side effects of antipsychotics are linked to their association kinetics at dopamine
809 D2 receptors. Nat Commun *8*, 763.

810 Trendelkamp-Schroer, B., and Noe, F. (2013). Efficient Bayesian estimation of Markov model
811 transition matrices with given stationary distribution. J Chem Phys *138*, 164113.
812 Vanommeslaeghe, K., Hatcher, E., Acharya, C., Kundu, S., Zhong, S., Shim, J., Darian, E.,
813 Guvench, O., Lopes, P., Vorobyov, I.*, et al.* (2010). CHARMM general force field: A force field
814 for drug-like molecules compatible with the CHARMM all-atom additive biological force fields. J
815 Comput Chem *31*, 671-690.
816 Venkatakrishnan, A.J., Deupi, X., Lebon, G., Tate, C.G., Schertler, G.F., and Babu, M.M. (2013).
817 Molecular signatures of G-protein-coupled receptors. Nature *494*, 185-194.
818 Wang, S., Che, T., Levit, A., Shoichet, B.K., Wacker, D., and Roth, B.L. (2018). Structure of the
819 D2 dopamine receptor bound to the atypical antipsychotic drug risperidone. Nature *555*, 269-
820 273.
821 Wang, S., Wacker, D., Levit, A., Che, T., Betz, R.M., McCorvy, J.D., Venkatakrishnan, A.J., Huang,
822 X.P., Dror, R.O., Shoichet, B.K.*, et al.* (2017). D4 dopamine receptor high-resolution structures
823 enable the discovery of selective agonists. Science *358*, 381-386.
824 Weis, W.I., and Kobilka, B.K. (2018). The Molecular Basis of G Protein-Coupled Receptor
825 Activation. Annu Rev Biochem *87*, 897-919.
826 Zhang, B., Albaker, A., Plouffe, B., Lefebvre, C., and Tiberi, M. (2014). Constitutive activities and
827 inverse agonism in dopamine receptors. Adv Pharmacol *70*, 175-214.

828 **FIGURES AND FIGURE LEGENDS**

829 **Figure 1.** The structures of homologous D_2R, D_3R, and D_4R show different conformations in the
830 extracellular vestibules. Superpositioning of D_2R, D_3R, and D_4R structures shows that the binding
831 of eticlopride (ETQ, cyan) in D_3R and nemonapride (NEMO, pale cyan) in D_4R result in outward
832 and inward rearrangements of the extracellular portions of TM5 and TM6, respectively, compared
833 to the binding of risperidone (RISP, orange) in D_2R.

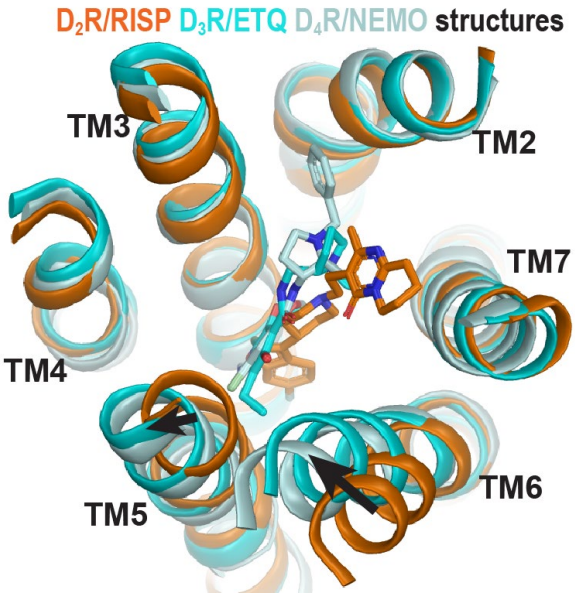

834 **Figure 2**. Divergent occupations of the Ile$^{3.40}$ sub-pocket by non-selective ligands from different
835 scaffolds. In the D_2R structure (**a**), the F-substitution on the benzisoxazole ring of risperidone
836 occupies the Ile$^{3.40}$ sub-pocket (dotted circle) enclosed by conserved Ile$^{3.40}$ (mutated to Ala in the
837 crystal structure to thermostabilize the receptor), Phe$^{5.47}$, and Phe$^{6.44}$. The same viewing angle
838 shows that in the D_3R (**b**) and D_4R (**c**) structures, Cys$^{3.36}$ rotates to fill in the Ile$^{3.40}$ sub-pocket, and
839 the substituted benzamides eticlopride and nemonapride cannot occupy the aligned sub-pockets.
840 In our D_2R/risperidone simulations (**d**), risperidone maintains its pose revealed by the crystal
841 structure. In the D_2R/spiperone simulations (**e**), the Ile$^{3.40}$ sub-pocket is similarly occupied as in
842 D_2R/risperidone. In the D_2R/eticlopride simulations (**f**), the Ile$^{3.40}$ sub-pocket is collapsed as in the
843 D_3R (**b**) and D_4R (**c**) structures (this trend is independent of the force field being used in the
844 simulations).

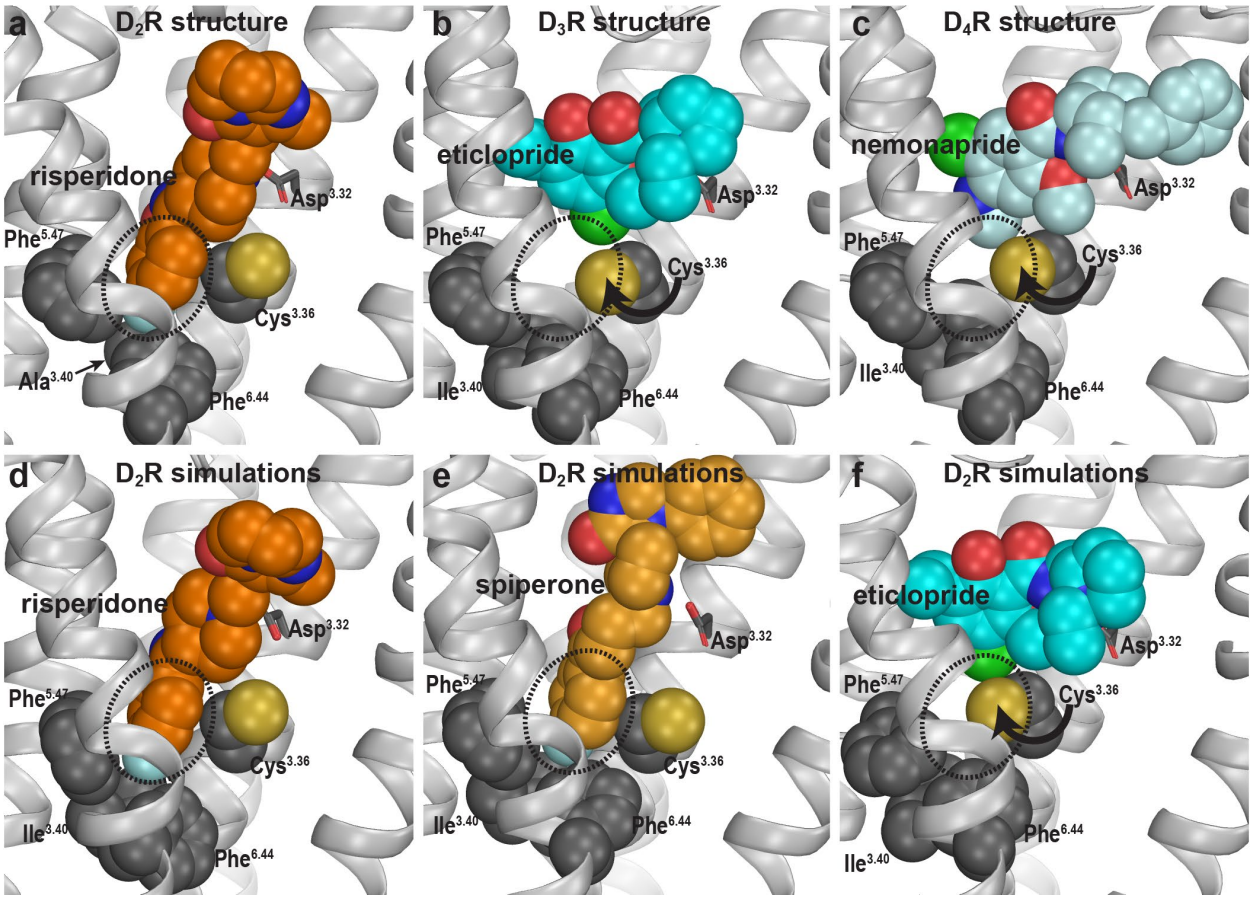

845 **Figure 3.** The extent of inverse agonism is negatively related with the Na^+ sensitivity of ligand
846 binding. In a D_2R-Go BRET assay, the maximal responses of the indicated ligands are normalized
847 to that of the reference full agonist quinpirole. The ligands that are insensitive to Na^+ in D_2R
848 binding display significantly higher inverse agonism (in each case, **P<0.0001 using ordinary
849 one-way ANOVA followed by Tukey's multiple comparisons test) than the Na^+-sensitive ligands;
850 however, within the Na^+-sensitive group, raclopride is significantly different from eticlopride
851 (P=0.005).

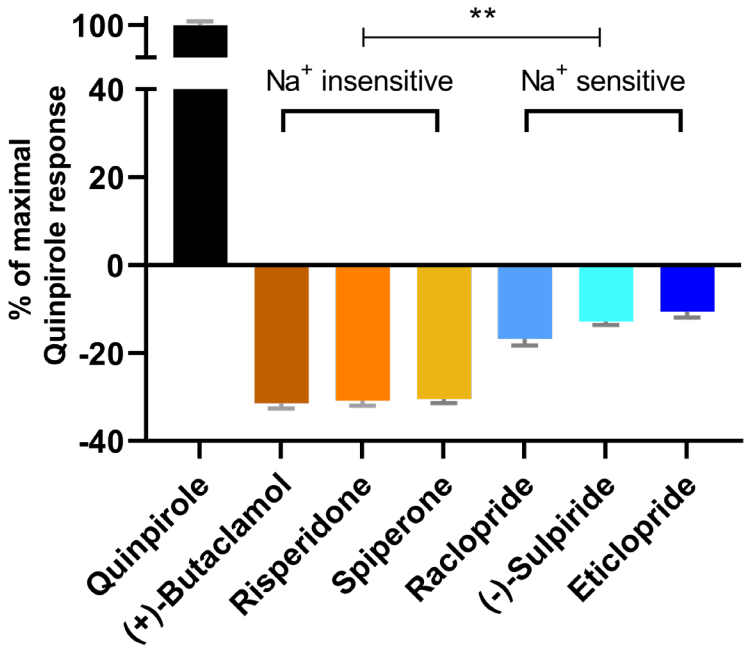

852 **Figure 4.** The different conformations in the extracellular vestibules of D_2R and D_3R are likely due
853 to binding of non-selective ligands from different scaffolds. (**a**) superpositioning of representative
854 frames of the D_2R/ETQ and D_2R/RISP simulations shows a similarly trend of the outward and
855 inward movements of TM5 and TM6, respectively, in the presence of the bound ETQ, even when
856 the simulations were started from the D_2R conformation stabilized by RISP. Note Ser193$^{5.42}$ and
857 Ser194$^{5.43}$ would clash with the bound eticlopride if there was conformational adjustment. (**b**, **c**)
858 PIA-GPCR analysis (see Methods) comparing the D_2R/ETQ and D_2R/RISP conformations. The
859 analysis of the pairwise-distance differences among the subsegments (**b**) indicates that TM6e
860 moves inward (smaller distance to TM2e, dark red pixel), while TM5e moves outward (larger
861 distances to TM7e, dark blue pixel) in the D_2R/ETQ simulations. The analysis of pairwise-distance
862 differences among the Cα atoms of the ligand binding residues (**c**) indicates significant changes
863 near residues Phe189$^{5.38}$, Ser193$^{5.42}$, Asn367$^{6.58}$, and Ile368$^{6.59}$ (darker colored pixels).

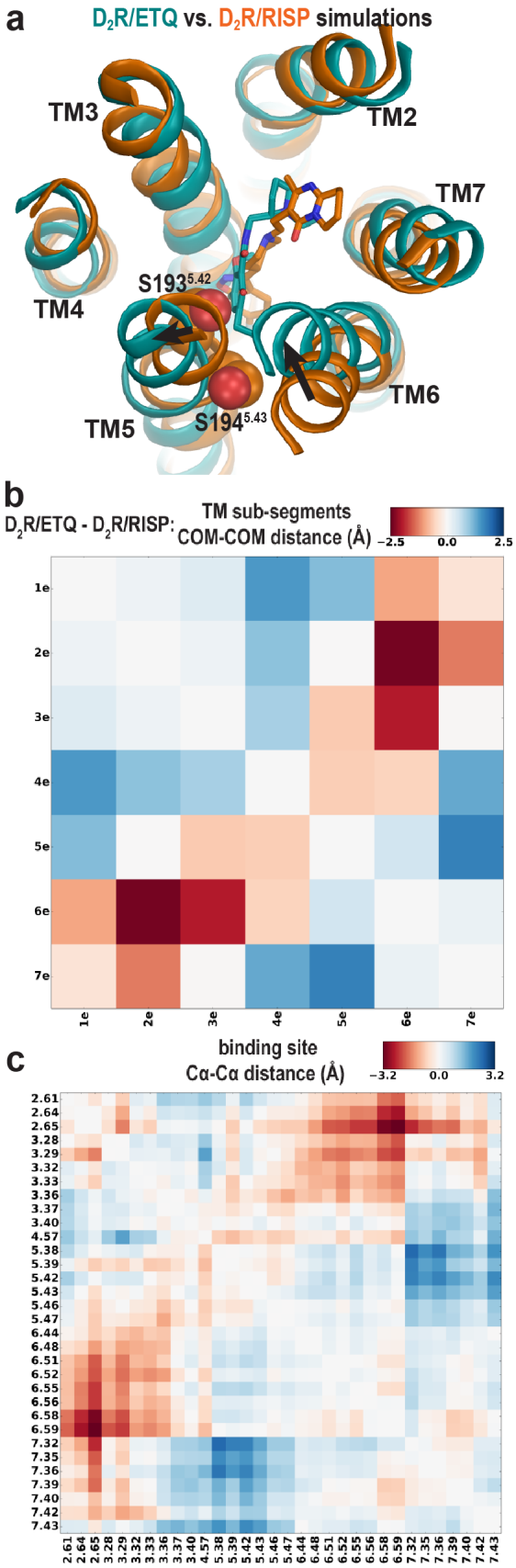
a
D2R/ETQ vs. D2R/RISP simulations
TM3
TM2
TM7
TM4
S193 5.42
TM6
TM5
S194 5.43
b
D2R/ETQ - D2R/RISP:
TM sub-segments
COM-COM distance (Å)
−2.5
0.0
2.5
1e
2e
3e
4e
5e
6e
7e
c
binding site
Cα-Cα distance (Å)
−3.2
0.0
3.2
2.61
2.64
2.65
3.28
3.29
3.32
3.33
3.36
3.37
3.40
4.57
5.38
5.39
5.42
5.43
5.46
5.47
6.44
6.48
6.51
6.52
6.55
6.56
6.58
6.59
7.32
7.35
7.36
7.39
7.40
7.42
7.43

864 **Figure 5**. The helical conformation of EL2 in the D_2R/risperidone structure has a tendency to
865 unwind in our simulations, regardless of the bound ligand. (**a**) The Ile183$^{EL2.51}$-Asn186$^{EL2.54}$
866 backbone H-bond and the Ile183$^{EL2.51}$-Asp108$^{3.26}$ interaction in D_2R and their aligned interactions
867 in D_3R. (**b**) the scatter plots of the two distances in the indicated D_2R and D_3R complexes. The
868 orange and cyan crosses indicated the distances in the D_2R/risperidone and D_3R/eticlopride
869 structures, respectively. (**c**) The distributions of the EL2.51-EL2.54 distances in the indicated
870 simulations. These distances were used to evaluate the tendency to unwind using Markov state
871 model (MSM) analysis in **d**. (**d**) The MSM analysis of the transition between the helical and
872 extended conformational states of EL2. The area of each disk representing a state is proportional
873 to the equilibrium probability (π) in each simulated condition. The values from the maximum
874 likelihood Bayesian Markov model for π and transition rates from 500 Bayesian Markov model
875 samples are shown. Thus, EL2 in all the D_2R complexes show significant tendencies to unwind,
876 while that in D_3R/eticlopride remains extended.

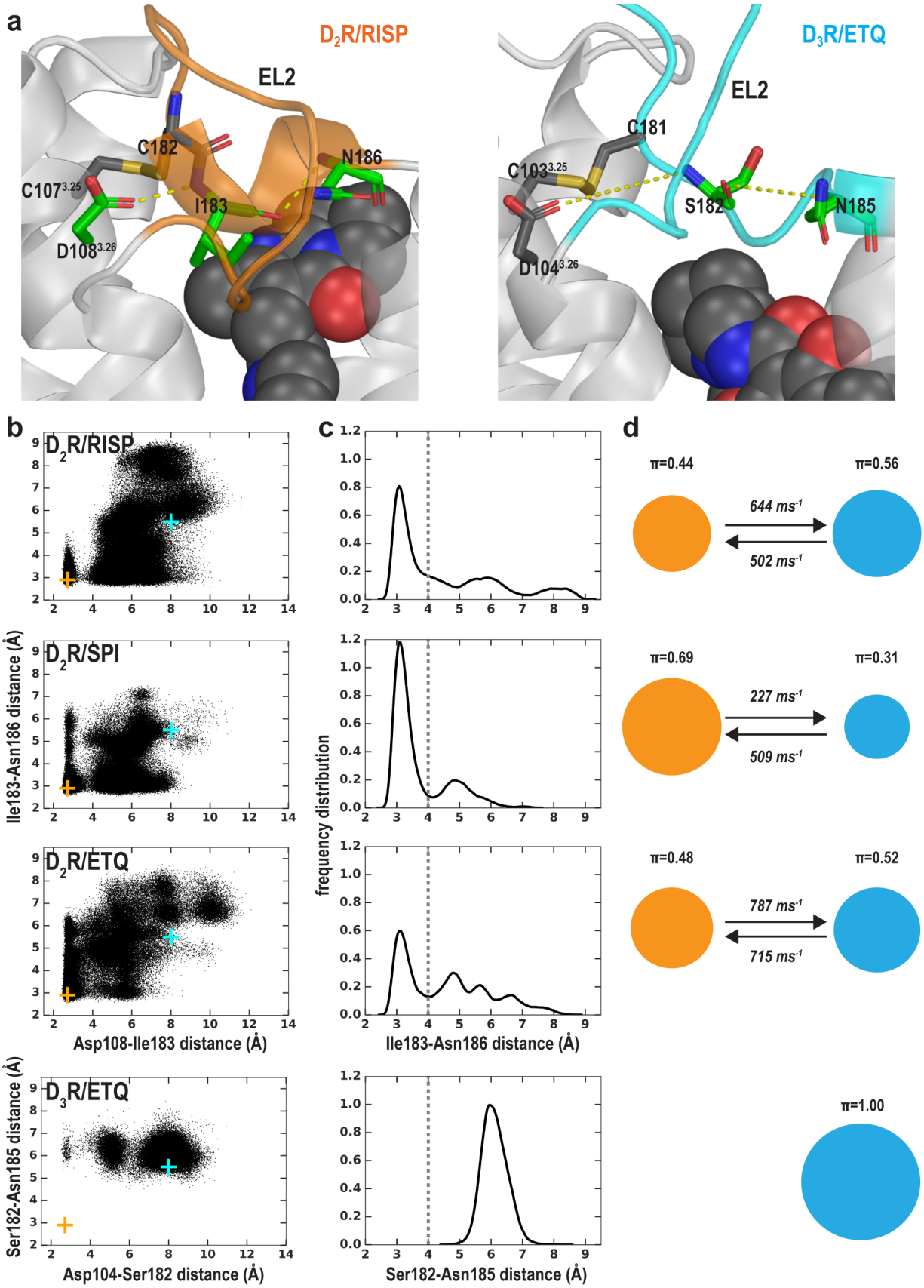
a
D2R/RISP
EL2
C182
N186
C107 3.25
I183
D108 3.26
D3R/ETQ
EL2
C181
C103 3.25
S182
N185
D104 3.26
b
D2R/RISP
D2R/SPI
D2R/ETQ
D3R/ETQ
Ile183-Asn186 distance (Å)
Asp108-Ile183 distance (Å)
Ser182-Asn185 distance (Å)
Asp104-Ser182 distance (Å)
c
frequency distribution
Ile183-Asn186 distance (Å)
Ser182-Asn185 distance (Å)
d
π=0.44
π=0.56
644 ms-1
502 ms-1
π=0.69
π=0.31
227 ms-1
509 ms-1
π=0.48
π=0.52
787 ms-1
715 ms-1
π=1.00

877 **Figure 6**. The EL2 conformation affects the EL1 conformation. Divergent EL1-EL2 interfaces
878 among the D_2R (**a**), D_3R, and D_4R (**b**) structures. In the D_2R structure, the Trp100$^{EL1.50}$ in EL1 only
879 forms a weak interaction with Ile184$^{EL2.52}$; while the aligned Trp96$^{EL1.50}$ of D_3R and Trp101$^{EL1.50}$ in
880 D_4R are stabilized by their interactions with the disulfide bond – their passages towards the
881 position of Trp100$^{EL1.50}$ in D_2R are blocked by the extended EL2. In our simulations, Trp100$^{EL1.50}$
882 in D_2R shows significant flexibility and can adopt multiple positions and orientations in
883 D_2R/risperidone (**c**), while Trp96$^{EL1.50}$ in D_3R is highly stable in D_3R/eticlopride (**d**). (**e**) The χ1 and
884 χ2 dihedral angles of Trp100$^{EL1.50}$ in the subset of the D_2R/risperidone simulations in which EL2
885 is still in a helical conformation (orange), are more widely distributed than those of Trp96$^{EL1.50}$ in
886 the D_3R/eticlopride simulations in which EL2 remains in extended conformations (cyan). These
887 dihedral angle values in the D_2R and D_3R structures are indicated with the orange and cyan stars,
888 respectively. (**f**), For the same two sets of simulations in **e**, the distance between the center of
889 mass (COM) of the sidechain heavy atoms of Trp100 in D_2R and the COM of the Cα atoms of the
890 ligand binding site residues (excluding Trp100, see Methods for the list of the residues) has wider
891 distributions than the corresponding distance between Trp96$^{EL1.50}$ in D_3R and its ligand binding
892 site. These distances in the D_2R and D_3R structures are indicated with the orange and cyan dotted
893 lines, respectively.

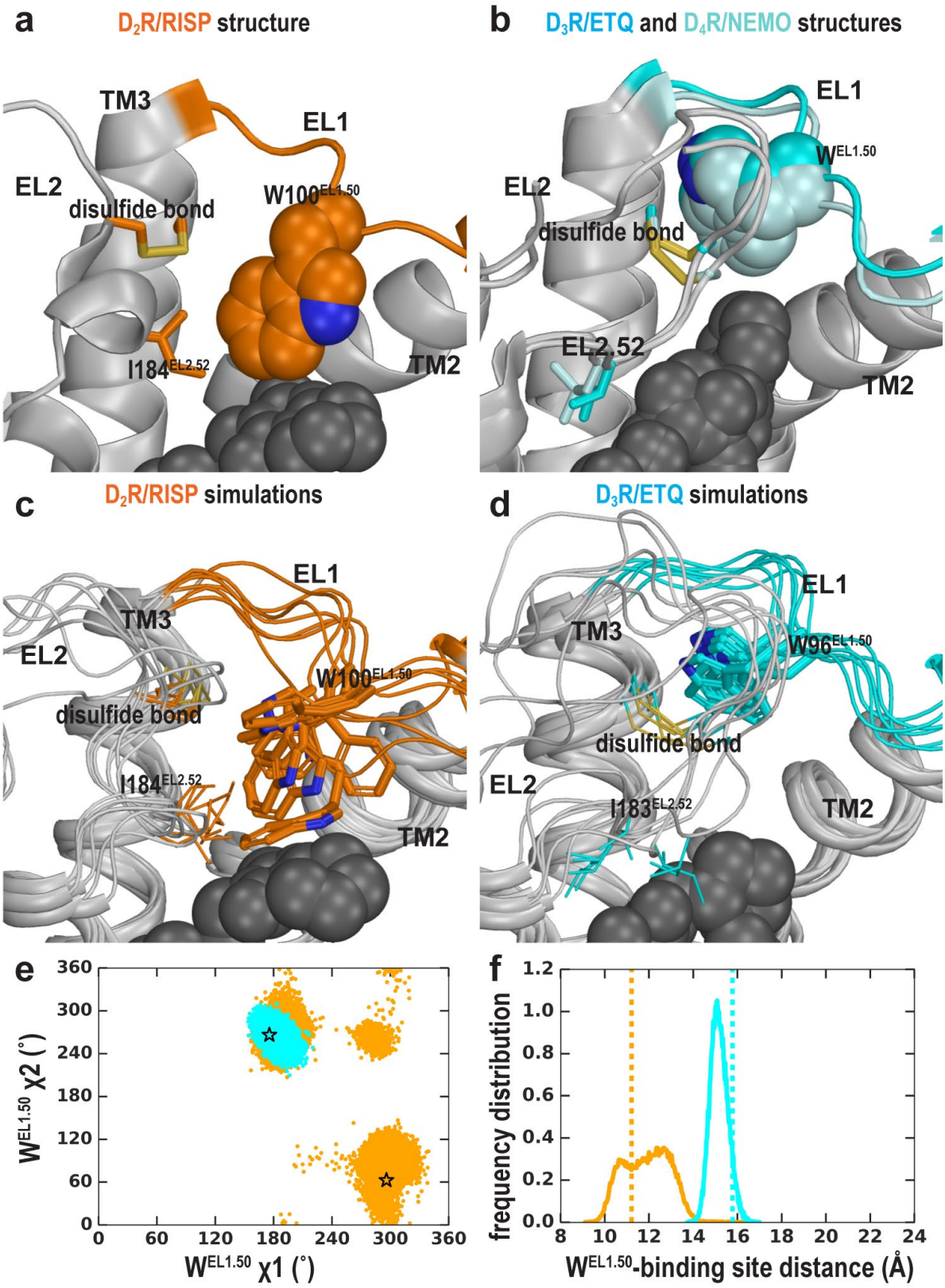
a
D2R/RISP structure
TM3
EL1
EL2
disulfide bond
W100EL1.50
I184EL2.52
TM2
b
D3R/ETQ and D4R/NEMO structures
EL1
WEL1.50
EL2
disulfide bond
EL2.52
TM2
c
D2R/RISP simulations
EL1
TM3
EL2
W100EL1.50
disulfide bond
I184EL2.52
TM2
d
D3R/ETQ simulations
EL1
TM3
W96EL1.50
disulfide bond
EL2
I183EL2.52
TM2
e
WEL1.50 χ2 (°)
WEL1.50 χ1 (°)
0
60
120
180
240
300
360
f
frequency distribution
WEL1.50-binding site distance (Å)
0.0
0.2
0.4
0.6
0.8
1.0
1.2
8
10
12
14
16
18
20
22
24

894 **Figure 7**. The average pairwise RMSDs of the clusters of the OBS conformations. The clustering
895 level was chosen to be 4, so that the average pairwise RMSDs (apRMSDs) between the
896 D_2R/eticlopride clusters (1 and 2, see Table 4 for the composition of each cluster) and
897 D_2R/risperidone clusters (3 and 4) are similar to that between D_2R and D_3R structures (1.2 Å),
898 while all the apRMSDs within a cluster are smaller than those between any given two clusters.

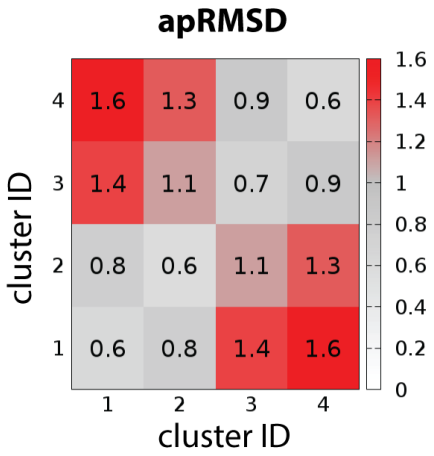

SUPPLEMENTARY INFORMATION

Figure 1 – figure supplement 1. Chemical structure alignments of the non-selective D_2-like receptors ligands. The moieties that occupy the $Ile^{3.40}$ sub-pocket are colored in orange.

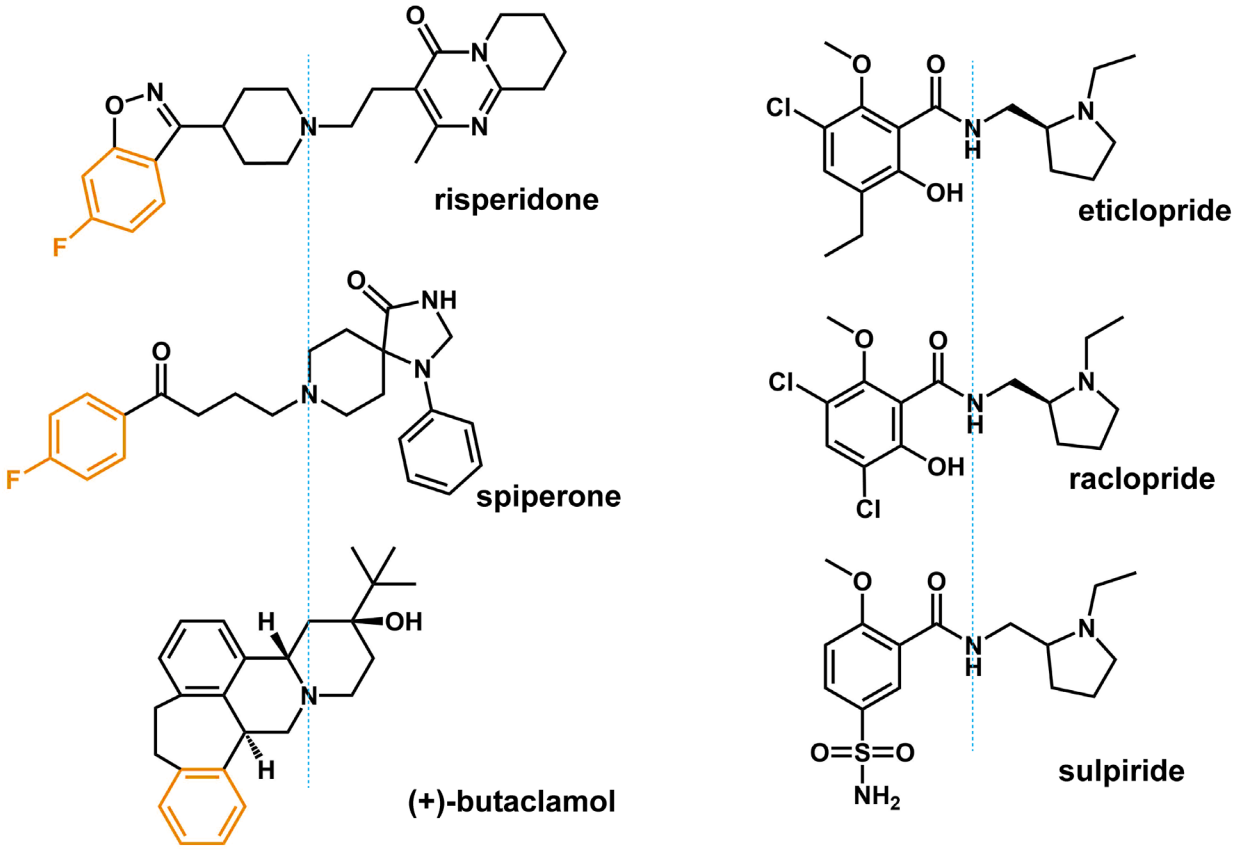

902 **Figure 2 – figure supplement 1**. Allosteric communication between the Ile$^{3.40}$ sub-pocket and
903 the Na^+ binding site. Risperidone (**a**, **b**) and spiperone (**d**, **e**) similarly occupy the Ile$^{3.40}$ sub-pocket
904 in both the presence and absence of Na^+ bound at the Asp80$^{2.50}$ site. In the eticlopride (**g**, **h**) and
905 (-)-sulpiride (**j**, **k**) bound conditions, the Ile$^{3.40}$ sub-pocket is not occupied, and Cys$^{3.36}$ shows
906 flexibility in the absence of bound Na^+. (**c**, **f**, **i**, and **l**) Distributions of the χ1 rotamer of Cys$^{3.36}$ in
907 the D_2R simulations in the presence of different bound ligands.

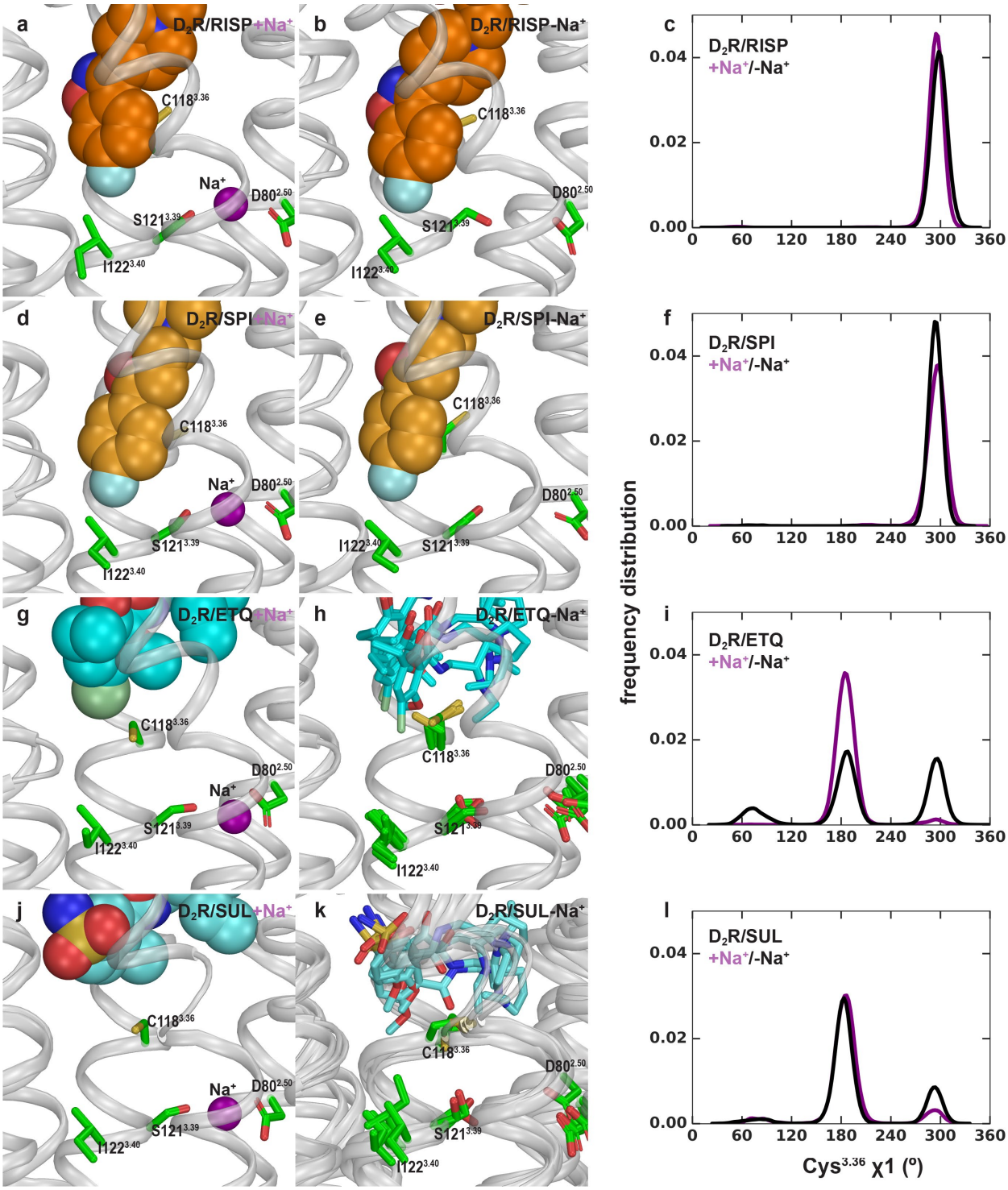
a
D2R/RISP+Na+
C118 3.36
Na+
D80 2.50
S121 3.39
I122 3.40
b
D2R/RISP-Na+
C118 3.36
D80 2.50
S121 3.39
I122 3.40
c
D2R/RISP
+Na+/-Na+
d
D2R/SPI+Na+
C118 3.36
Na+
D80 2.50
S121 3.39
I122 3.40
e
D2R/SPI-Na+
C118 3.36
D80 2.50
I122 3.40
S121 3.39
f
D2R/SPI
+Na+/-Na+
g
D2R/ETQ+Na+
C118 3.36
D80 2.50
Na+
S121 3.39
I122 3.40
h
D2R/ETQ-Na+
C118 3.36
D80 2.50
S121 3.39
I122 3.40
i
D2R/ETQ
+Na+/-Na+
j
D2R/SUL+Na+
C118 3.36
Na+
D80 2.50
S121 3.39
I122 3.40
k
D2R/SUL-Na+
C118 3.36
D80 2.50
S121 3.39
I122 3.40
l
D2R/SUL
+Na+/-Na+
frequency distribution
0.00
0.02
0.04
0
60
120
180
240
300
360
Cys 3.36 χ1 (º)

908 **Figure 4 – figure supplement 1.** The occupation of the Ile$^{3.40}$ pocket by risperidone is associated
909 with outward movement of the extracellular portion of TM6. (**a**) superpositioning of the
910 D_2R/risperidone and D_3R/eticlopride structures shows the occupation of the Ile$^{3.40}$ pocket by the
911 benzisoxazole moiety of risperidone directly affects the positioning of Phe$^{6.52}$, the impact of which
912 propagates to affect overall conformation of the extracellular portion of TM6. (**b**) Similar impact
913 was observed in the comparison of the results from the D_2R/risperidone and D_2R/eticlopride
914 simulations.

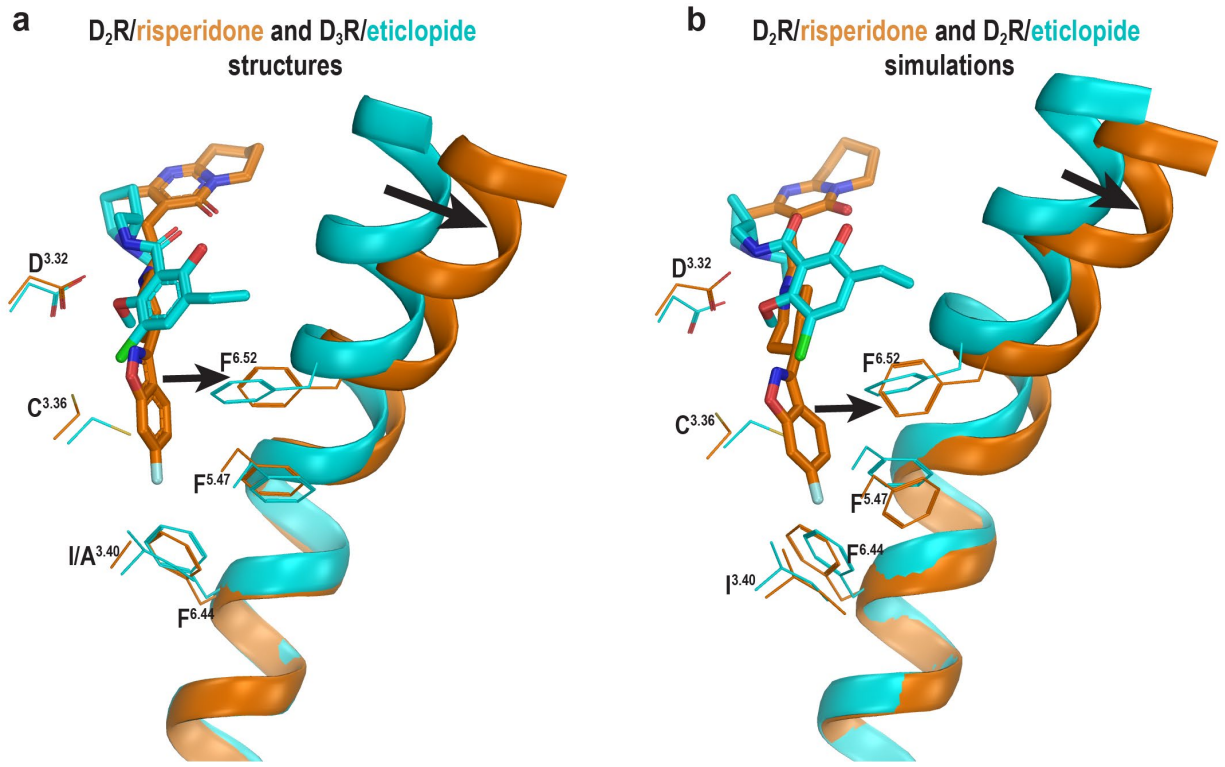

915 **Figure 5 – figure supplement 1**. Sequence alignment and residue indices of EL1 and EL2 for
916 the receptors being compared in this study. The positions with identical residues are in dark grey
917 shade, the conserved positions are in light grey shade.

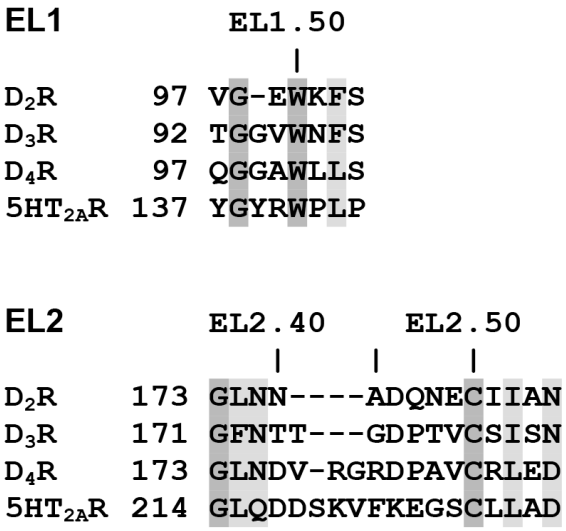

Figure 5 – figure supplement 2. The helical region of EL2 of D_2R can spontaneously unwind to an extended conformation similar to that of D_3R. (**a**) Residues $182^{EL2.50}$-$186^{EL2.54}$ in the D_2R/RISP structure are in a helical conformation. EL2 is connected to TM3 via a disulfide bond ($Cys182^{EL2.50}$-$Cys107^{3.25}$), while the backbone of $Ile183^{EL2.51}$ forms an interaction with $Asp108^{3.26}$ (magenta dotted line). (**b**) The key events in the EL2 unwinding pathway (for each step, a number of representative frames are shown): the ionic interaction between $Asp108^{3.26}$ and $Ile183^{EL2.51}$ has to dissociate first (**i**), which allows the sidechain of Ile183 to rotate towards lipids and pass through a minor barrier formed by $Gly173^{EL2.37}$ (**ii**); then the sidechain of $Ile183^{EL2.51}$ rotates towards the extracellular vestibule while that of $Ile184^{EL2.52}$ tilts under EL2 (**iii**); these changes allow $Asn175^{EL2.39}$ to move from facing lipid to facing the binding site (**iv**). The resulting conformation of EL2 of D_2R is similar to that of D_3R for all the aforementioned residues (**c**). In particular, $Asn173^{EL2.39}$ of D_3R, which aligns to $Asn175^{EL2.39}$ of D_2R, forms an H-bond interaction with $Asp104^{3.26}$.

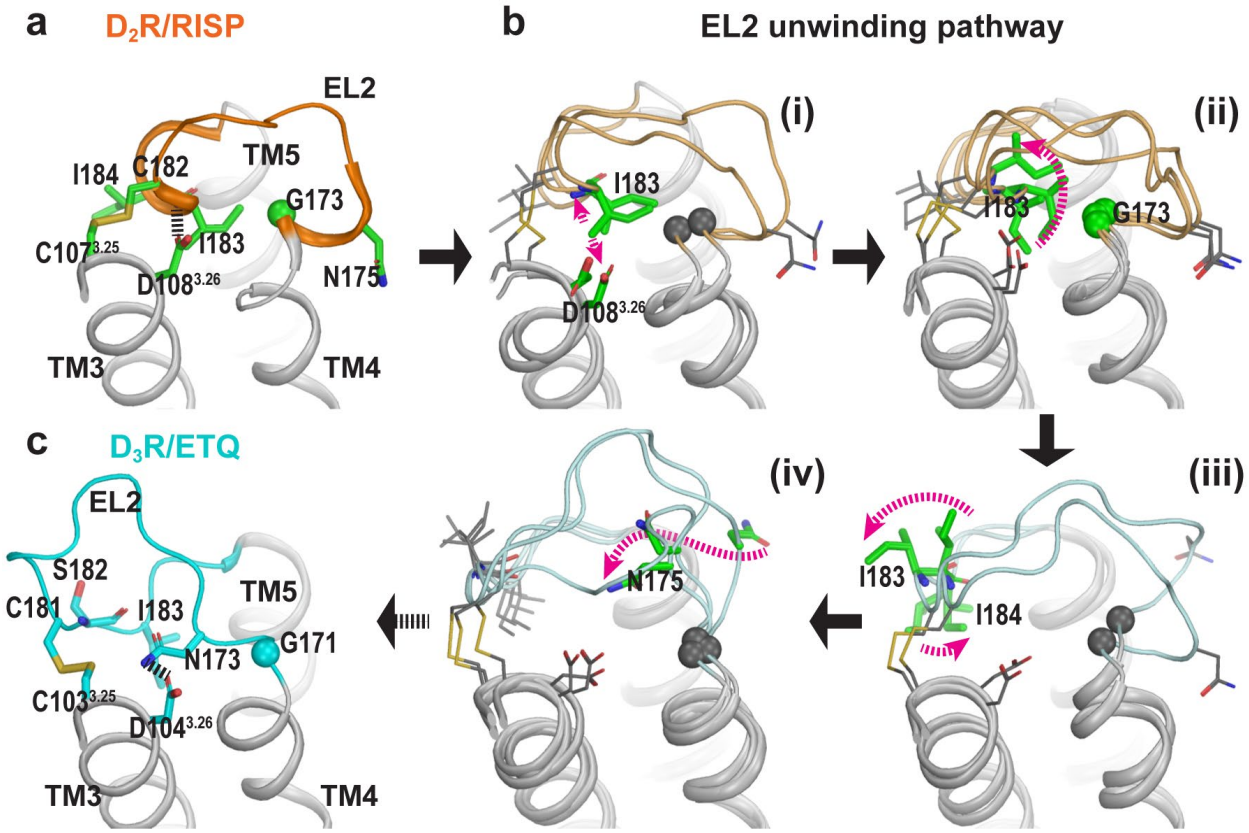

931 **Figure 5 – figure supplement 3**. The MSM analysis of Ile183-Asn186 distance in the simulations

932 of the D_2R/aripiprazole, D_3R/S22, and D_3R/R22 complexes (Table 1). The early stage of D_3R/S22

933 and D_3R/R22 simulations has been reported previously (Michino et al., 2017). The representation

934 and color scheme is the same as that for Figure 5.

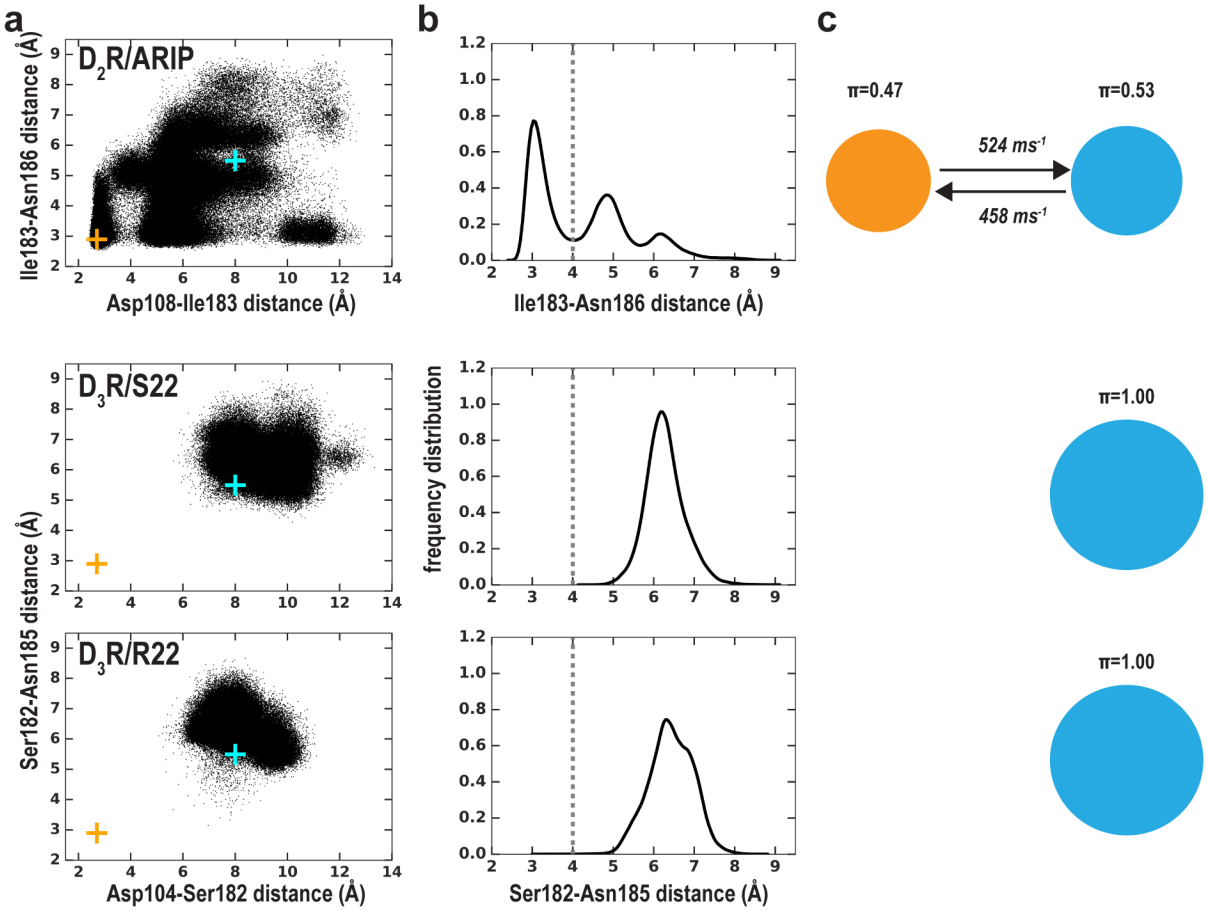

935 **Figure 5 – figure supplement 4**. The distinct D_2R EL2 conformations revealed by the MD
936 simulations are similar to those of homologous receptors. The C-terminal helical EL2
937 conformation in the D_2R structure (**d**) can be maintained in the simulations (**a**). the C-terminal
938 extended conformation (**b**) is similar to those in the D_3R structure (**e**). The N-terminal helical
939 conformation (**c**) is reminiscent of that in the 5-$HT_{2A}R$/risperidone structure (**g**), and those in β_1
940 and β_2 adrenergic receptors structures (not shown).

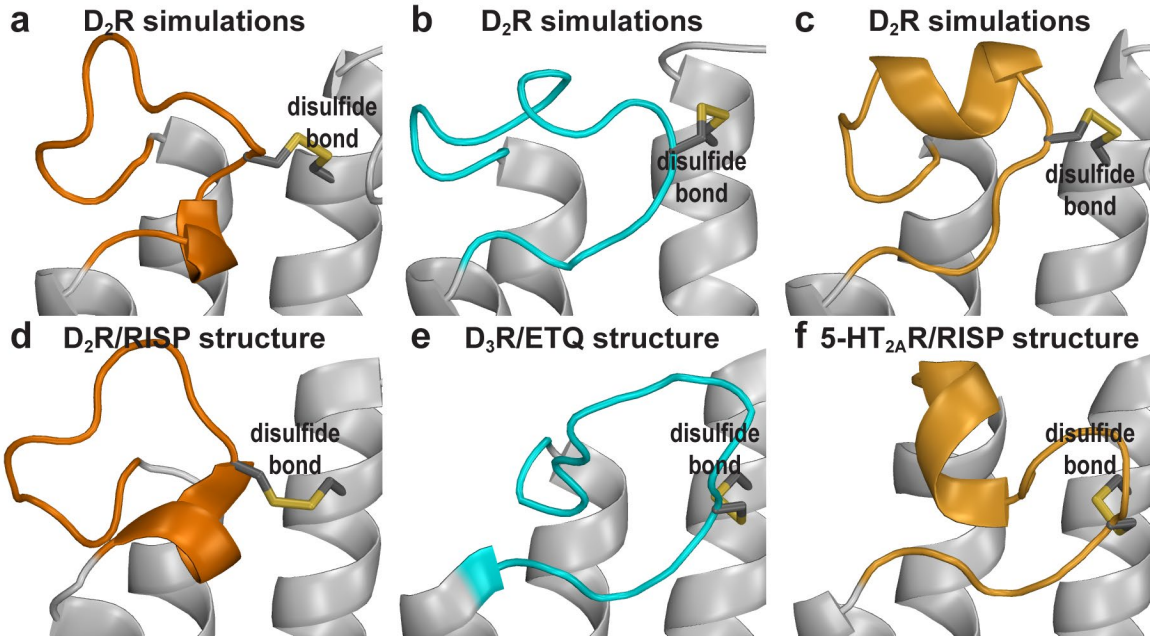

941 **Figure 5 – figure supplement 5**. The accessibility pattern of EL2 revealed by previous SCAM
942 studies in D_2R is more consistent with an extended EL2 conformation similar to that in the
943 D_3R/eticlopride structure. The accessible residues are in green, the protected residues are in cyan.
944 In the D_2R/risperidone structure (**a**), Ile183$^{EL2.51}$ blocks the accessibility of Gly173$^{EL2.37}$ to the OBS,
945 while Asn175 faces lipid. In the D_2R/eticlopride simulations (**b**) and D_3R/eticlopride structure (**c**),
946 Asn$^{EL2.39}$ rotates to point inward, while Ile183$^{EL2.51}$ in D_2R and Ser182$^{EL2.51}$ in D_3R rotates to face
947 the extracellular vestibule of the receptors.

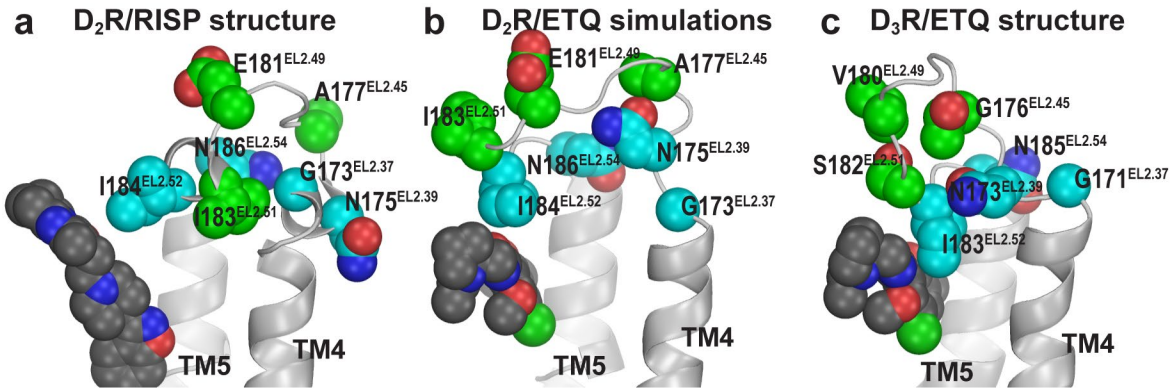

Figure 5 – figure supplement 6. Implied timescales (ITS) for the MSM analysis. The implied timescales (ITS) of the transition between the two states in each of the D_2R conditions shown in Figure 5 and Figure 5 – figure supplement 3 are plotted against various lag times. ITSs were not computed for D_3R conditions because there was not transition between two states. The ITS of the maximum likelihood Bayesian Markov model is shown in a blue solid line, whereas the means and the 95% confidence intervals (computed by Bayesian sampling) are shown in dashed and shaded areas, respectively. Timescales smaller than the lag time are shown in grey-shaded area. A lag time of 300 ns was chosen for our analysis.

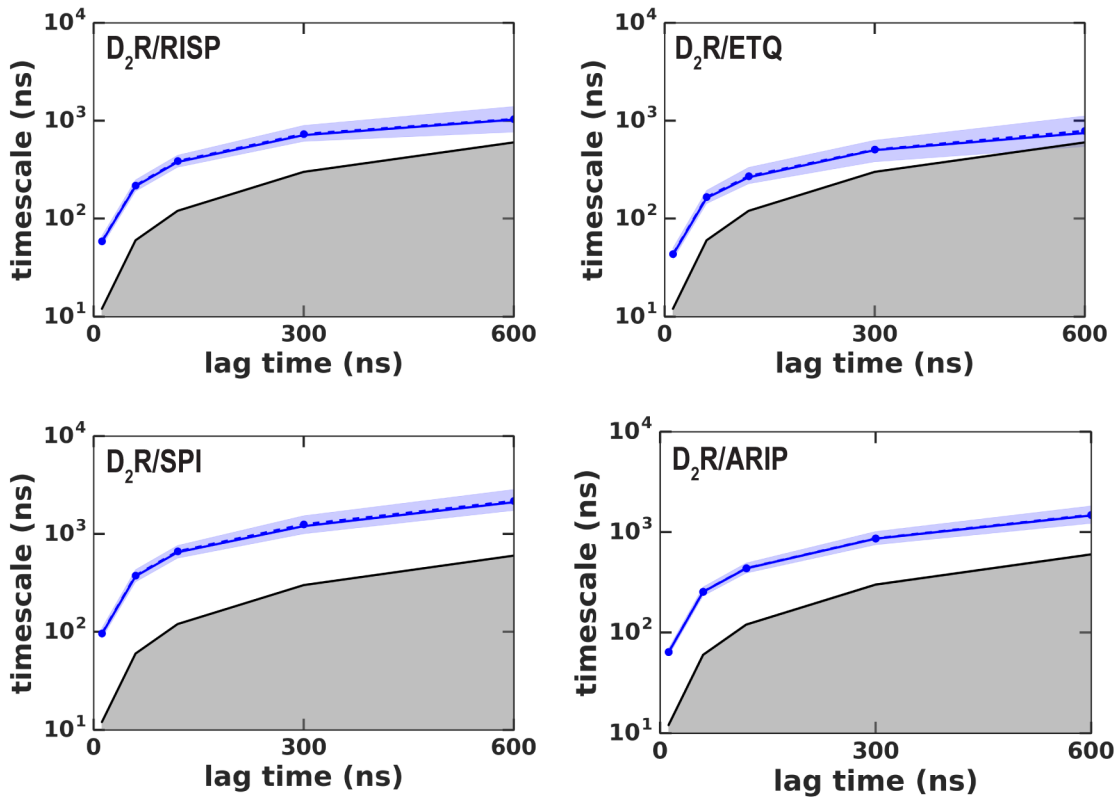

956 **Figure 6 – figure supplement 1.** EL1 is dynamic in the D_2R/eticlopride and D_2R/spiperone
957 simulations when EL2 is helical. Trp100 shows significant flexibility and can adopt multiple
958 positions and orientations in D_2R/eticlopride (**a-c**) and D_2R/spiperone (**d-f**) simulations. Their χ1
959 and χ2 dihedral angles of Trp100 (**b**, **e**) and the distance between Trp100 and the ligand binding
960 site (**c**, **f**) have wide and different distributions. These dihedral angle values in the D_2R and D_3R
961 structures are indicated with the orange and cyan stars, respectively. The distances in the D_2R
962 and D_3R structures are indicated with the orange and cyan dotted lines, respectively.

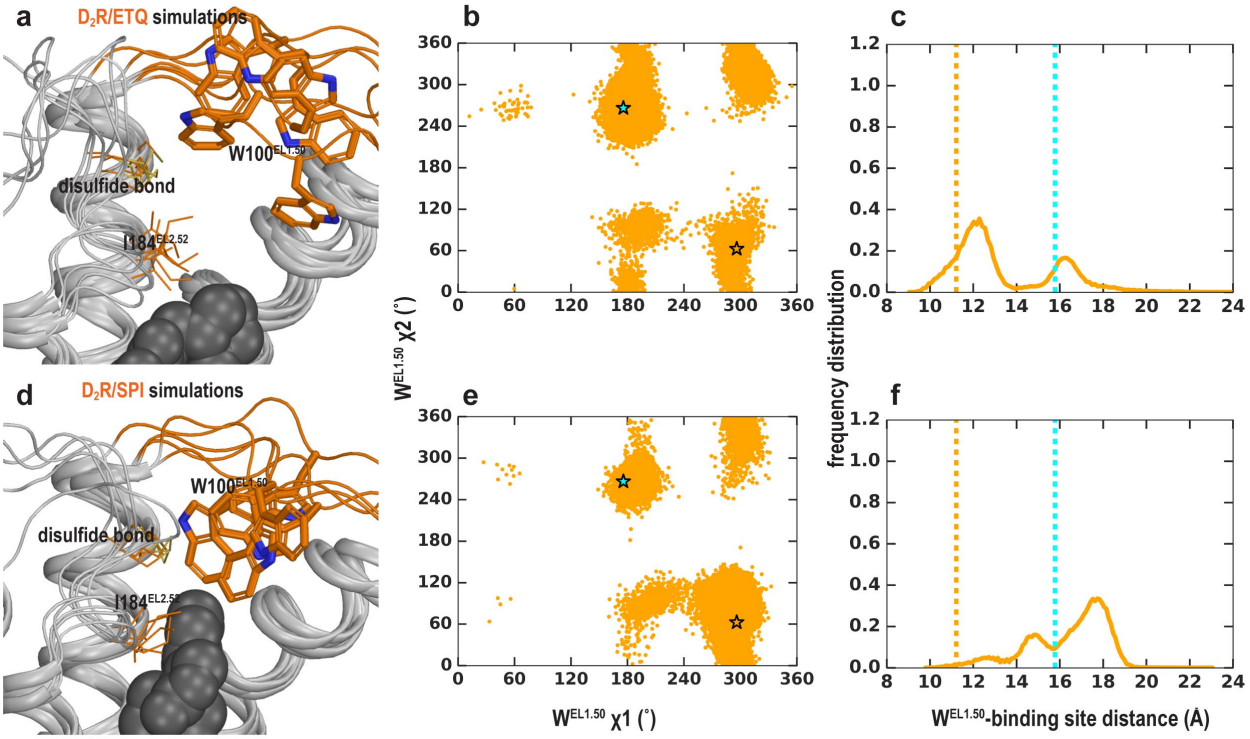

963 **Figure 6 – figure supplement 2**. Trp$^{EL1.50}$ is closely associated with Leu$^{2.64}$ regardless of the EL2
964 conformation. In the D_2R structure (**a**), the Trp100$^{EL1.50}$ in EL1 forms a weak interaction with
965 Ile184$^{EL2.52}$ when EL2 is helical, while the aligned Trp96$^{EL1.50}$ in the D_3R structure does not form
966 such an interaction with Ile183$^{EL2.52}$ and is stabilized by their interactions with the disulfide bond
967 of the extended EL2 (**b**). In both structures, Trp100$^{EL1.50}$ is in close association with Leu$^{2.64}$.

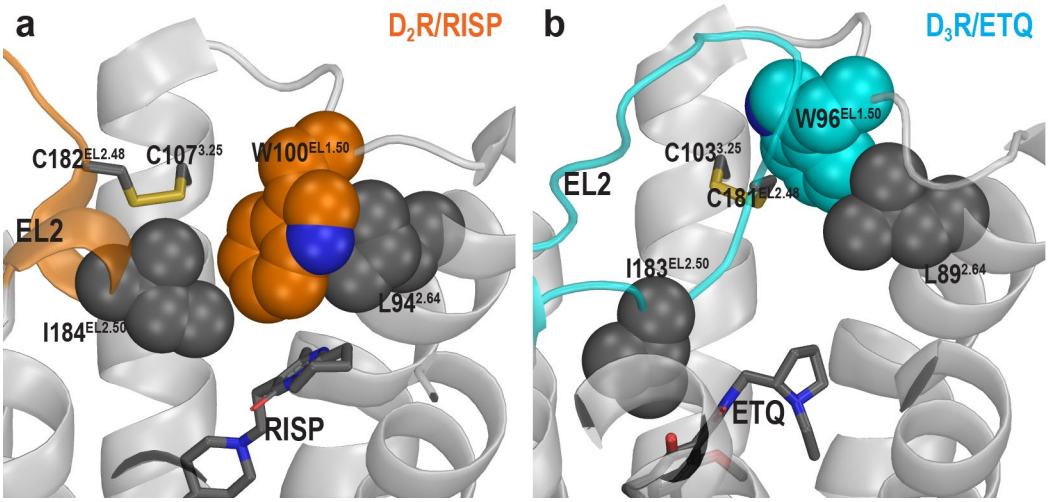

968

969 **Video 1.** A movie of a 4.2 μs D_2R/risperidone trajectory collected using the OPLS3 force field
970 shows spontaneous unwinding of EL2. The conformation of EL2 gradually transitions to an
971 extended configuration similar to that in the D3R structure. See Figure 5 – figure supplement 2
972 for the pathway of unwinding. Note that the extended conformation of EL2 stabilizes Trp100$^{EL1.50}$.
973 The Cα atom of Gly173$^{EL2.37}$, the sidechains of Trp100$^{EL1.50}$, Ile183$^{EL2.51}$, and Ile184$^{EL2.52}$ and the
974 bound risperidone are shown as spheres. Asp108$^{3.26}$ and the disulfide bond between Cys107$^{3.25}$
975 and Cys182$^{EL2.50}$ are shown as sticks. The carbon atoms of Gly173$^{EL2.37}$ and Ile184$^{EL2.52}$ are
976 colored in cyan, those of Ile183$^{EL2.51}$ are in green, those of Trp100$^{EL1.50}$, Cys107$^{3.25}$, Asp108$^{3.26}$,
977 Asn175$^{EL2.39}$, and Cys182 $^{EL2.50}$ are in dark grey; those of the bound ligand risperidone are in
978 orange.
979 **Video 2**. A movie of a 4.2 μs D_2R/eticlopride trajectory shows the dynamics of Trp100$^{EL1.50}$ when
980 the C-terminal portion of EL2 is in a helical conformation. Note that Trp100$^{EL1.50}$ can be stabilized
981 by interacting with the disulfide bond. The presentation and color scheme are similar to those in
982 Video 1, except that the bound carbon atoms of the ligand eticlopride are colored in cyan.
983 **Video 3**. A movie of a 3.6 μs D_2R/eticlopride trajectory collected using the CHARMM36 force field
984 shows another example of unwinding of EL2. Thus, considering the similar unwinding pathway
985 as that in Video 1 (Figure 5 – figure supplement 2), the unwinding does not depend on the force
986 field used in the simulations or the identity of the antagonist bound in the OBS. Note the sidechain
987 of Asn175$^{EL2.39}$ rotates inward and approaches Asp108$^{3.26}$ in this trajectory. The presentation and
988 color scheme are the same as those in Video 2.
989 **Video 4.** A movie of a 4.5 μs D_2R/risperidone trajectory shows the N-terminal portion of EL2 can
990 transition into a helical conformation when the C-terminal portion is extended. This is a novel EL2
991 conformation that has not been revealed by the D_2R, D_3R or D_4R structures but similar to those
992 in the 5-$HT_{2A}R$/risperidone (Figure 5 – figure supplement 4f), β_2AR and β_2AR structures. The
993 presentation and color scheme are the same as those in Video 1.